We are IntechOpen, the world's leading publisher of Open Access books Built by scientists, for scientists

4,800
Open access books available

122,000
International authors and editors

135M
Downloads

Our authors are among the

154
Countries delivered to

TOP 1%
most cited scientists

12.2%
Contributors from top 500 universities

WEB OF SCIENCE™

Selection of our books indexed in the Book Citation Index in Web of Science™ Core Collection (BKCI)

Interested in publishing with us?
Contact book.department@intechopen.com

Numbers displayed above are based on latest data collected.
For more information visit www.intechopen.com

Chapter 5

Rare-earth Element-bearing Apatites and Oxyapatites

Petr Ptáček

Additional information is available at the end of the chapter

http://dx.doi.org/10.5772/62209

Abstract

A number of prepared alkaline-earth-rare-earth silicates and germanates also have the structure of apatite type. The fifth chapter of this book then continues with description of synthetic compounds of apatite structure. Attention will be directed to description of rare-earth element bearing apatites and oxyapatites. The structure, properties and preparation of apatite-type silicates, germanates and borates were described. This chapter gives also description of oxygen-rich apatites, which are promising material for electrolytes in solid oxide fuel cells and sensors and explain the basic concepts between structure and conductivity of these compounds. The additional information about application of apatites is given in the last chapter of this book. Furthermore, N-apatite, REE vanadocalcic apatite and apatite type yttrium phosphates were described.

Keywords: Apatite, Oxyapatite, Conductivity, Silicates, Germanates, Borates, N-apatite, Apatite-type yttrium phosphates

In this chapter, the preparation and the properties of synthetic phases of apatite are given; the geological role is described in **Section 7.3**. The ideal general formula of an apatite-type oxide may be written as $M_{10}(XO_4)_6O_2$ (M = alkaline-earth and/or rare-earth element, X = Si, Ge, P, V, …). The structure (**Fig. 1**) can be described in terms of a "microporous"[1] [1] framework ($A(1)_4(XO_4)_6$) composed of face sharing $M(1)O_6$ trigonal meta-prismatic columns, which are corner connected to MO_4 tetrahedra. This framework allows some flexibility to accommodate remaining $M(2)_6O_2$ units [2].

[1] Microporous material is defined as containing pores with the diameters >2 nm. The materials with the pore diameter in the range from 2 to 50 nm and higher than 50 nm are termed as mesoporous and macroporous, respectively. In combination with nanotechnology, the term nanoporous material is often used. Despite the fact that there is not clear definition, usually the pores with the size from 0.1 to 100 nm are considered. In other words, nanoporous covers the range from microporous to macroporous [1].

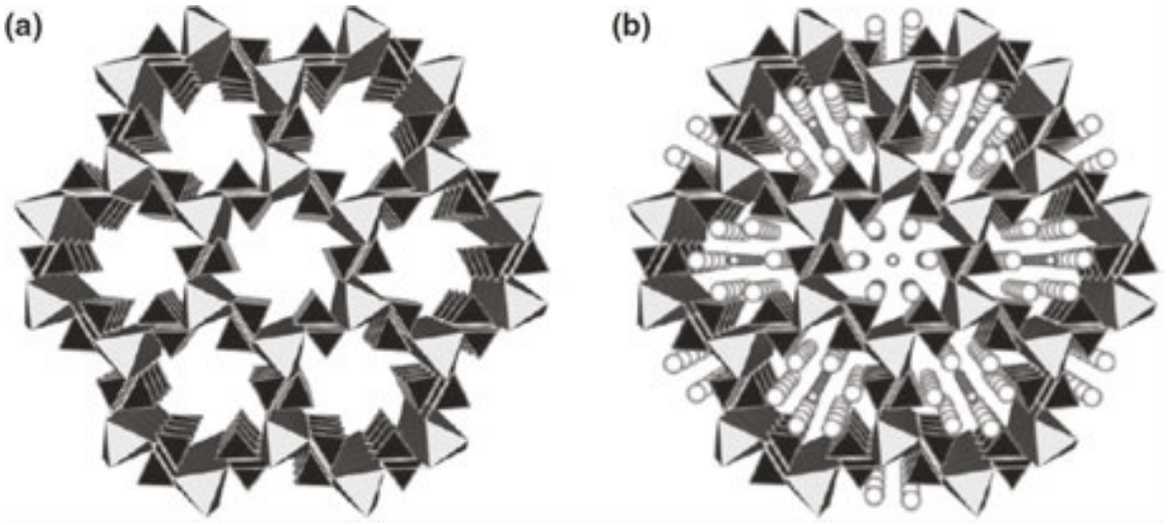

Fig. 1. Illustration of "microporous" $M(1)(XO_4)_6$ framework of the apatite ($M_{10}(XO_4)_6O_2$) structure (a): tetrahedra MO_4, M(1) cation at the center of trigonal meta-prism. Remaining $M(2)_6O_2$ units occupy the cavities within this framework (b): large spheres are M(2) cations and small spheres are O anions [2].

5.1 Apatite-type lanthanium silicates

During recent decades, oxyapatite[2]-type structure with the general formula: $REE_{9.33+x}Si_6O_{26+3x/2}$ (where REE is rare-earth element) [3],[4], $REE_{9.33}\square_{0.67}(SiO_4)_6O_2$ [5] or $REE_{10-x}(SiO_4)_6O_{2+y}$ [6] has attracted considerable attention as oxide ion conductors. Apatite-type oxides have attracted much attention as the material for electrolytes in solid oxide fuel cell and sensors (**Chapter 10**).

In low atomic number rare-earth silicate systems, an apatite phase occurs with a range of stability extending from $Ln_{4.67}(SiO_4)_3O$ to $Ln_4(SiO_4)_3$. The stability decreases as the rare-earth atomic number increases, with a mixture of Ln_2SiO_5 and $Ln_2Si_2O_7$ replacing apatite as the preferred phase assemblage [7],[8],[9],[10],[11].

Apatite-type rare-earth element (REE) silicates of the composition of $REE_{10-x}(SiO_4)_6O_{2+y}$, where REE = La, Nd, Gd and Dy, were prepared by Martínez-González et al [6] via the mechano-chemical synthesis (stabilized zirconia planetary ball mill: ball-to-powder ratio ~10:1, 350 rpm for maximum time of 9 h) starting from the stoichiometric mixtures of constituent oxides, REE_2O_3 and SiO_2 (molar ratio = 4:5), followed by post-milling thermal treatment (1500°C for 3 h). The ionic conductivity increases with the increasing size of REE cations.[3] The mechano-

[2] Since the prefix "oxy-" can be explained as containing oxygen or additional oxygen, and the prefix "oxo-" is used for the functional group or substituent oxygen atom connected to another atom by a double bond (=O), the names oxyapatite, oxy-apatite, oxoapatite and oxo-apatite can be considered as synonyms. In the published literature, the name oxyapatite is the most frequently used (~90%), and the term oxy-apatite is the second (~8%). The names oxoapatite and oxo-apatite are used much rarely (only about ~2%).

Apatite-type silicates described in this chapter can be also named as oxy-britholites (oxybritholites) [84].

[3] This conclusion is in discrepancy with the findings of Higuchi et al [12] described below.

http://dx.doi.org/10.5772/62209

chemical synthesis of apatite-type lanthanum silicates from the mixture of La_2O_3 and amorphous silica without post-milling thermal treatment was described by Fuentes et al [4].

Rare-earth element-doped apatite-type lanthanum silicates of the composition of $La_9MSi_6O_{27}$, where M = Nd, Sm, Gd and Yb, were synthesized by the high-temperature solid-state reaction process by Xiang et al [3]. All rare-earth oxide powders (La_2O_3, Nd_2O_3, Sm_2O_3, Gd_2O_3 and Yb_2O_3) were firstly pre-calcined at 900°C for 2 h in order to achieve complete decarbonation and dehydroxylation before weighing. The stoichiometric mixtures were mechanically mixed in absolute ethanol for 24 h using zirconia milling media at the speed of 400 rpm and dried at 100°C in air. The powder mixture was calcined at 1350°C for 10 h and then ground by hand with an agate mortar and pestle to reduce the particle size. After that, the powders were uniaxially pressed at 20 MPa and then statically cold pressed at 200 MPa for 5 min. The compacts were pressureless sintered at 1650 K for 10 h in air.

Apatite-type phase	**Lattice parameters [Å]**		***M***	***V***	**Density**	***E***	σ_0
	a	***c***	**[g·mol^{-1}]**	**[Å^3]**	**[g·cm^{-3}]**	**[eV]**	**[S·K·cm^{-1}]**
$La_4SiO_3O_{12}$	9.376	6.761	831.87	514.73	—	—	—
$La_{10}Si_6O_{27}$	9.709	7.176	1989.552	585.82	5.168	0.76	$2.51\cdot10^4$
$La_9NdSi_6O_{27}$	9.729	7.191	1994.886	589.46	5.344	0.79	$4.78\cdot10^4$
$La_9SmSi_6O_{27}$	9.692	7.161	2001.046	582.55	5.405	0.82	$1.85\cdot10^4$
$La_9GdSi_6O_{27}$	9.723	7.187	2007.896	588.41	5.485	0.87	$3.24\cdot10^4$
$La_9YbSi_6O_{27}$	9.701	7.143	2023.686	582.16	5.459	0.98	$4.34\cdot10^5$

Table 1. The properties of apatite-type lanthanium silicates [3],[8].

The lattice parameters and the properties of prepared apatite-type lanthanium silicates are listed in **Table 1**. All prepared compounds possess hexagonal apatite structure with the space group $P6_3/M$. The temperature dependence of total electrical conductivity for different compositions is determined using the Arrhenius equation[4] [13],[14],[15] in the following form [3],[5],[16],[17]:

$$\sigma\ T = \sigma_0\ \exp\left(-\frac{E}{k_B T}\right) = \sigma_0\ \exp\left(-\frac{\Delta H_m + \Delta H_a}{k_B T}\right) \quad (1)$$

where σ is the total electrical conductivity, σ_0 is the pre-exponential factor related to the effective number of mobile oxide ions, E is the activation energy for the electrical conduction process, k_B is the Boltzmann constant and T is absolute temperature. ΔH_m and ΔH_a denote the

[4] The equation of Svante August Arrhenius [13],[14], which predicts that the rate constant k depends on the temperature: $k = A\ exp\ (-E_a/RT)$, where A is the frequency (pre-exponential factor), E_a is the activation energy, R is universal gas constant (8.314 J·K^{-1}·mol^{-1}) and T is the thermodynamic temperature [13].

migration enthalpy of oxygen ion and the association enthalpy of defects, respectively. The determined activation energy and pre-exponential factor are listed in **Table 1**. It can be seen that the activation energy gradually increases from $La_{10}Si_6O_{27}$ to $La_9GdSi_6O_{27}$. Total electrical conductivity can be calculated from the following equation:

$$\sigma = \frac{h}{RS} \tag{2}$$

where *h* is the thickness of the specimen, *S* is the electrode area of the specimen surface and *R* is the total resistance including grain and grain boundary resistance. Lanthanum silicates doped with Nd or Yb cations exhibit higher total electrical conductivity than undoped lanthanum silicates. The highest total conductivity value obtained at 500°C is $4.31 \cdot 10^{-4}$ S·cm^{-1} for $La_9NdSi_6O_{27}$. The total electrical conductivity is also a function of partial pressure of oxygen [3].

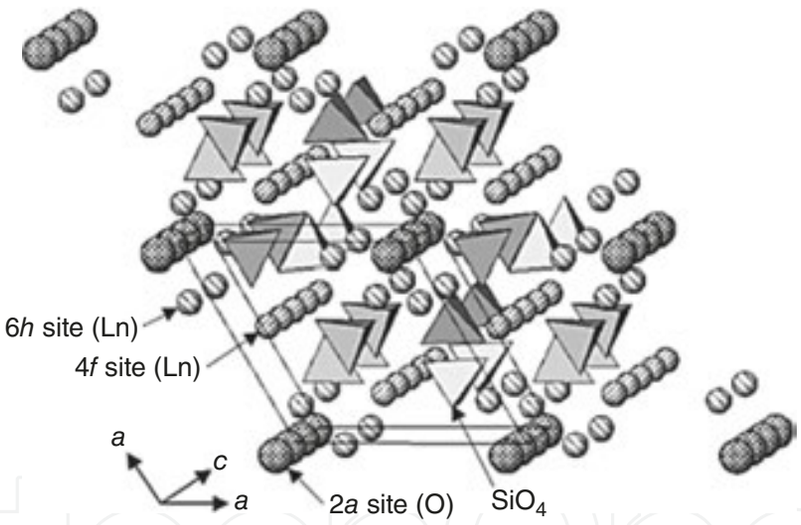

Fig. 2. Crystal structure of apatite-type rare-earth element silicate viewed along the c-axis [12].

The measurements using single crystals revealed definite anisotropy of the electrical conductivity of $Ln_{9.33}(SiO_4)_6O_2$, that is, the conductivity parallel to the c-axis is larger by one order of magnitude than that perpendicular to the c-axis. This fact clearly indicates that the channel oxide ions not bonded to silicon are the principal charge carriers in apatite-type lanthanum silicates. The structure of apatite-type rare-earth silicate is shown in **Fig. 2**. SiO_4 tetrahedra are isolated mutually, and Ln ions (REE ions, in general) at 6*h* sites (sevenfold coordinated site (x,y,¼)) [18][5] form channels, in which oxide ions at 2*a* sites are located (possess the threefold coordination with rare-earth ions at the 6*h* sites in the same plane), along the c-axis.

http://dx.doi.org/10.5772/62209

These mobile ions at these sites have much larger anisotropic displacement parameters in the direction of the c-axis than those in the direction of the a-axis, even at room temperature, which reflects high oxide ion conduction along the c-axis. The ninefold coordinate position (4*f* site (1/3,2/3,*z*)) is the second site for the accommodation of REE cations in the structure of apatite-type REE silicate [6],[12],[19],[20].

Since the interstitial space provided by these rare-earth ions is the smallest throughout the channel along the c-axis of the apatite structure, the migration of oxide ions through the channel will not be affected significantly even if the sizes of rare-earth ions are varied. It is therefore reasonable that the electrical conductivities of apatite-type rare-earth silicates are independent on the kind of rare-earth elements [12].

Conventional oxide ion conductors are designed on the basis of the oxygen vacancy model by the introduction of aliovalent[6] [21] cations. In $Ln_{9.33}(SiO_4)_6O_2$, however, cation vacancies are present rather than oxygen vacancies. Therefore, the introduction of cation vacancies into the structure of an oxide material may induce high oxide ion conductivity if the structure has a channel or a plane that can be a path for the migration of oxide ions [12].

Apparent exchange of O(1), O(2) and O(3) oxide ions bonded to Si was observed by ^{17}O NMR measurement on $La_{9.33}Si_6O_{26}$ by KIYINO et al [22], while it was not observed for oxide ion on the isolated site O(4). The results indicate that oxide ions bonded to Si at the position O(1), O(2) and O(3) are the main diffusion species in the oxide ion conductivity.

Trivalent and divalent dopants[7] [23] have been introduced into the $La_{9.33}(SiO_4)_6O_2$ structure according to the following nominal mechanisms [24]:

$$Si^{4+} \rightarrow M^{3+} + \frac{1}{3}La^{3+} \tag{3}$$

$$\frac{2}{3}La^{3+} \rightarrow AEE^{2+} \tag{4}$$

$$\frac{1}{3}La^{3+} \rightarrow AEE^{2+} + \frac{1}{2}O^{2-} \tag{5}$$

[5] According to the WYCKOFF notation: the specification of actual coordinates of atoms within the unit or primitive cell, which can be generated by the point-group operations or may be found by reference in the International Tables for Crystallography [18].

[6] Cation with different valence. Apatite structure shows large flexibility upon the substitution of other aliovalent cations at the 'Ca' sites, pentavalent and tetravalent ions such as V^{5+}, As^{5+} and Si^{4+} at the 'P' site and halide, oxide ions at the 'OH' site [21], as was described.

[7] Dopants are also termed as doping agents. It can be defined as an impurity element added to the material structure in low concentration (usually <1 wt.% [23]) in order to alter its properties.

where M = Al, Ga, B, Co, Fe, Mn, … and AEE denotes the alkaline-earth elements (Ca, Sr and Ba). Doping with Al, Ga and B according to the formula: $La_{9.33+x/3}(SiO_4)_{6-x}(MO_4)_xO_2$, via the mechanism in **Eq. 3**, causes that bulk conductivity increases in up to two orders of magnitude in the case of Al for $x = 1 – 1.5$. If, however, the sample is stoichiometric on both cation and anion sites, as for $La_8Sr_2(SiO_4)_6O_2$, the AEE doping reduces the conductivity and increases the activation energy for the conduction compared to $La_{9.33}(SiO_4)_6O_2$.

The effect of Fe doping on the electrical properties of lanthanum silicates of the composition of $La_{10}Si_{6-x}Fe_xO_{27-x/2}$ (where $x = 0.2, 0.4, 0.6, 0.8$ and 1.0) was performed by SHI and ZHANG [16] via the sol-gel process. Tetraethyl orthosilicate (TEOS), $La(NO_3)_3{\cdot}6H_2O$ and $Fe(NO_3)_3{\cdot}9H_2O$ were used as starting materials. Stoichiometric amounts of $Fe(NO_3)_3{\cdot}9H_2O$ and $La(NO_3)_3{\cdot}6H_2O$ were dissolved in the mixture of ethanol, acetic acid and distilled water. The appropriate amount of TEOS was added to the solution while continuous stirring. The solution became gradually a purple clear sol. After refluxing at 80°C for 1 – 2 h, the sol transferred to a clear gel. Then, the wet gel was dried at 100°C for 20 h. The gel was heated at 600°C for 4 h to remove water and organic components and to decompose nitrates. In order to get the desired phase, obtained precursor was then calcined at 1000°C for 4 h.

Apatite-type lanthanium silicate	**Lattice parameters [Å]**		***V***	***E* (600 – 800°C)**	***E* (400 – 550°C)**
	a	***c***	**[Å³]**	**[eV]**	
$La_{10}Si_{5.8}Fe_{0.2}O_{26.9}$	9.725	7.192	589.1	0.78	0.96
$La_{10}Si_{5.6}Fe_{0.4}O_{26.8}$	9.729	7.208	590.8	0.74	0.95
$La_{10}Si_{5.4}Fe_{0.6}O_{26.7}$	9.732	7.220	592.2	0.72	0.89
$La_{10}Si_{5.2}Fe_{0.8}O_{26.6}$	9.735	2.217	592.3	0.74	1.01
$La_{10}Si_5FeO_{26.5}$	9.743	7.229	593.5	0.75	1.02

Table 2. Lattice parameters of Fe-doped apatite-type lanthanium silicates [16].

All synthesized samples have hexagonal lattice structure with the space group of $P6_3/M$. The lattice parameters of prepared Fe-doped apatite-type lanthanium silicates and the activation energy of conductivities (**Eq. 1**) for different Fe contents are listed in **Table 2**. When $x = 0.6$, $La_{10}Si_{5.4}Fe_{0.6}O_{26.7}$ exhibits the lowest activation energy. The lattice parameters of $La_{10}Si_6O_{27}$ (**Table 1**) and doped specimen (**Table 2**) show that the values of ***a***, ***c*** and ***V*** increase with the content of iron. The conductivity of $La_{10}Si_{6-x}Fe_xO_{27-x/2}$ is independent of oxygen partial pressure in the range from 0 to 100 kPa, which indicates that the conductivity of all samples is mainly ionic [16].

The oxygen ionic and electronic transport in apatite ceramics with the composition of $La_{10}Si_{6-x}Fe_xO_{27-x/2}$ ($x = 1 – 2$) [25] and $La_{10-x}Si_{6-y}Al_yO_{27-3x/2-y/2}$ ($x = 0 – 33$; $y = 0.5 – 1.5$) [26],[27] was investigated by SHAULA et al In both cases, the essential role of oxygen content on the ionic conductivity of apatite phase was recognized. The ion transference number[8] [28] increases with decreasing partial pressure of oxygen. Such behavior indicates that the conduction under

http://dx.doi.org/10.5772/62209

oxidizing condition is predominantly of p-type[9] (with respect to n-type of conductivity). Similar to the foundation of SHI and ZHANG [16], the conductivity of these phases is predominantly ionic and almost independent on partial pressure of oxygen. The ion transference numbers are higher than 0.99, while the p-type electronic contribution to total conductivity is about 3% (700 – 950°C, $La_{10}Si_4Fe_2O_{26}$). The oxygen ionic conductivity should increase with decreasing iron content due to higher concentration of oxygen interstitials.

Another important factor influencing the oxygen diffusion is M-site deficiency, which affects the unit cell volume and may cause the O(5) ion displacement into interstitial sites, thus creating the vacancies in the O(5) sites at fixed total oxygen content. In particular, an enhanced ionic conduction was found in the system $La_{9.33+x/3}Si_{6-x}Al_xO_{26}$, where Al doping is compensated by the A-site vacancy concentration without oxygen content variations [29],[30].

The incorporation of praseodymium in the apatite-type lattice of $La_{9.83-x}Pr_xSi_{4.5}Fe_{1.5}O_{26+\delta}$ (x = 0 – 6) decreases the unit cell volume, suppresses the Fe^{4+} formation according to Mössbauer spectroscopy[10] [31],[32],[33],[34] and increases p- and n-type electronic contributions to total conductivity under oxidizing conditions, while the level of oxygen ionic transport at temperatures above 1000 K remains unaffected [35].

Since the size of the conduction channel increases with the Mg doping, the enhancement of the ionic conductivity of lanthanum silicate-based apatites can be reached by optimizing the La content and the Mg doping level at the same time. The ionic conductivities of $La_{10}Si_{5.8}Mg_{0.2}O_{26.8}$ and $La_{9.8}Si_{5.7}Mg_{0.3}O_{26.4}$ at 800°C are 88 and 74 $mS \cdot cm^{-1}$ with the activation energy of 0.43 and 0.42 eV, respectively [36].

The ionic conduction in cation-deficient apatite $La_{9.33-2x/3}M_xSi_6O_{26}$, where M = Mg, Ca and Sr was investigated by YUAN et al [37]. The nature of dopant and the extent of substitution have a significant effect on the conductivity. The greatest decrease in conductivity is observed for Mg doping followed by Ca- and Sr-doped apatites. The effect is ultimately attributed to the amount of oxygen interstitials, which is affected by the crystal lattice distortion arising from the cation vacancies.

The incorporation of additional La_2O_3 into $La_{9.33}(SiO_4)_6O_2$ to form $La_{10}(SiO_4)_6O_3$ or intermediate compositions can most obviously be achieved by filling empty interstitial sites with oxygen. The only alternative scenario would involve the creation of cation vacancies on the Si sublattice, which is unlikely as Si is present as a complex anion. The incorporation of excess of La_2O_3 into $La_{9.33}(SiO_4)_6O_2$ can therefore be expressed as [10]:

---

[8] The fraction of total current that is transferred by a given ion is affected by its mobility. The sum of transport numbers for all ions in electrolyte is equal to one [28].

[9] The p-type carriers possess typically higher mobility [25].

[10] The technique is based on the Mössbauer effect of recoil-free nuclear resonance fluorescence [31], i.e. the phenomenon of emission or absorption of X-ray photon without the loss of energy. The Mössbauer effect has been detected in a total of 88 X-ray transitions in 72 isotopes of 42 different elements [32]. The ^{57}Fe Mössbauer isotope is the most frequently used [33]. The Mössbauer spectroscopy can be used to determine the oxidation states of iron in minerals and to identify the presence of some mineral species in samples of unknown composition [31].

$$La_{9.33}[\ ]_{0.67}(SiO_4)_6O_2 + 1/3\ La_2O_3 \rightarrow La_{10}(SiO_4)_6O_2O_i\left(La_{10}(SiO_4)O_3\right) \quad (6)$$

Thus, in the ideal pure $La_{10}(SiO_4)_6O_3$, the 4*f* and 6*h* sites are fully occupied by La^{3+} ions, while an extra oxygen interstitial is introduced into the lattice to maintain the electroneutrality. The oxygen interstitial may benefit the oxide ion transportation if it is located nearby the [001] direction c-axis of the conventional unit cell. From the space-filling consideration, the most appropriate sites for the oxygen occupation are in this position; however, some distortion of the O 2*a* sites would be required to accommodate extra oxygen atoms. This could be achieved by decreasing the symmetry from $P6_3/M$ to $P6_3$ allowing oxygen to move from 0,0,1/4 to 0,0,x. Recent studies suggest that a range of partially occupied (0,0,x) sites may accommodate this extra interstitial oxygen. From this point of view, $La_{10}(SiO_4)_6O_3$ should exhibit higher conductivity than $La_{9.33}(SiO_4)_6O_2$ [10],[38].

Introducing Sr^{2+} cations to the La^{3+} atomic positions, as in the $La_{10}(SiO_4)_6O_3$ phase, leads to complete elimination of vacancies according to the substitution [39]:

$$La_{10}(SiO_4)_6O_3 \overset{+Sr^{2+}}{\rightarrow} La_9Sr_1(SiO_4)_6O_{2.5} \overset{+Sr^{2+}}{\rightarrow} La_8Sr_2(SiO_4)_6O_2 \quad (7)$$

The substitution of La_2O_3 by SrO, taking into account the charge balance and the oxygen content, can be represented as follows (KRÖGER-VINK notation[11] [40],[41]):

$$SrO + 1/2\ O_o^x + La_{La}^x \rightarrow Sr_{La}^{/} + 1/2\ V_o^{\cdot\cdot} + 1/2\ La_2O_3 \quad (8)$$

Lanthanum oxyapatite phases are substantially stable with respect to their binary oxides. The general trend in the formation enthalpies as a function of (La + Sr)/(La + Sr + Si) shows that the apatite phase becomes more energetically stable as the cation vacancy and oxygen excess concentrations decrease. The stoichiometric sample achieved by Sr^{2+} doping, with no cation vacancies or interstitial oxygen atoms, is the most stable composition. The energetics of lanthanum silicate apatite materials ($La_{9.33+x}(SiO_4)_6O_{2+3x/2}$ and $La_{10-x}Sr_x(SiO_4)_6O_{3-0.5x}$) depends on lanthanum deficiency and oxygen interstitial[12] [42],[43] concentrations, and the cation vacancy concentrations appear to be the dominant factor in energetics [39].

[11] The KRÖGER-VINK notation indicates the lattice position for the point defect species in the crystal and its effective electric charge relative to the perfect lattice: $\mathbf{M}_Y^{\ Z}$ is the atomic species **M** (or vacancy **V**) that occupies the lattice site **Y** and possesses the effective charge **Z**, where the symbols ●, ' and × are used for the effective charge +1, -1 and neutral particle, respectively) [40]. For example, $\mathbf{Al}_i^{\bullet\bullet\bullet}$ is Al^{3+} ion at interstitial site (*i*), $\mathbf{V_{Al}}'''$ is Al^{3+} vacancy, $V_O^{\bullet\bullet}$ is O^{2-} vacancy, Sr_{La}' (**Eq. 8**) means Sr^{2+} ion replacing La^{3+} at lattice site, $Ti_{Al}^{\bullet}$ means Ti^{4+} replacing Al^{3+} at lattice site, ***e***' is electron and $\boldsymbol{h}^{\bullet}$ is the hole. The equation must fulfill the following three rules: mass balance (1), electroneutrality or charge balance (2) and site ratio conservation balance (3) [41].

[12] Interstitial sites are sites between normal (equilibrium) atomic positions of ideal lattice atoms [42]. Interstitial atoms and vacancies (lattice site where atom is absent) are the simplest types of point defects in a crystal. A vacancy and interstitial atoms positioned close together are referred to as the Frenkel pair. Apart from the point defects, the line crystal defects (dislocation and disclination) are recognized [43].

http://dx.doi.org/10.5772/62209

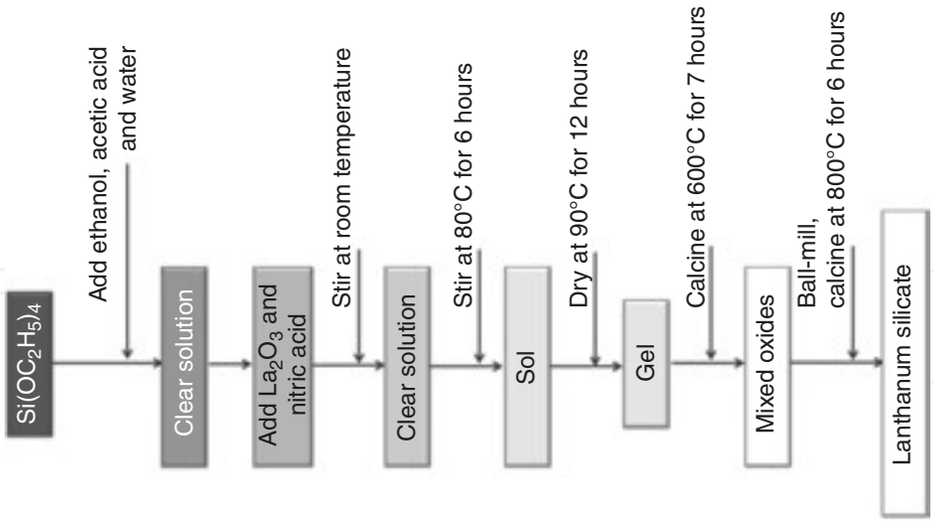

Fig. 3. Schematic diagram of preparation of lanthanum silicate by a sol-gel process [44].

The schematic diagram of the sol-gel process used by Tao and Irvine [44] for the preparation of apatite-type lanthanium silicates is shown in **Fig. 3**. The room-temperature structure is hexagonal, the space group is $P6_3$ or $P6_3/M$, with $a = 9.722$ and $c = 7.182$ Å for $La_{10}(SiO_4)_6O_3$ and $a = 9.717$ and $c = 7.177$ Å for $La_{9.33}(SiO_4)_6O_2$, i.e. the cell volume of $La_{10}(SiO_4)_6O_3$ is a little greater than that of $La_{9.33}(SiO_4)_6O_2$. Both compositions exhibit high ionic conductivity, although the grain boundary resistance is the dominant feature in the impedance spectrum of both. In general, the conductivity of $La_{10}(SiO_4)_6O_3$ is higher than that of $La_{9.33}(SiO_4)_6O_2$ and this indicates that oxygen interstitials may be introduced into the apatite lattice of $La_{10}(SiO_4)_6O_3$, which may benefit the oxygen ion transportation [44].

The $La_{10}Si_6O_{27}$ nanopowders with apatite structure were synthesized by the Li et al [45] co-precipitation method. After the calcination at 900°C and then removing of La_2O_3 by acid washing, the pure stoichiometric $La_{10}Si_6O_{27}$ nanopowders are obtained. The oxyapatite ceramics with the density higher than 95% can be obtained at rather low sintering temperature of 1300°C, and it has comparable total conductivity with the samples sintered at 1650°C from the powders prepared by solid-state reaction.

La_2O_3 and TEOS in stoichiometric amount were used by Masubuchi et al [46] as the starting materials for the preparation of both powder and film of apatite-type $La_{9.33}(SiO_4)_6O_2$ via the alkoxide hydrolysis. Lanthanum oxide was dissolved in HNO_3 (6 mol·dm^{-3}) and mixed with ethanol. Then, stoichiometric amount of TEOS in ethanol was added (La:Si = 9.33:6) to this solution. The precursor solution was obtained by refluxing for one night. This solution was heated to gelating on the hot plate followed by calcination and annealing in powder preparation. Either quartz glass or Pt foil substrate was dipped to the gelatinous solution and dried for the film preparation. It was calcined at 500°C for 1 h to remove the organic contents and then fired at 1000°C for 10 h. This preparation steps were repeated to increase the film thickness. The film showed preferred orientation of the apatite crystal in thinner film. The conductivity of sintered body was lower in about one order of magnitude than the value of single crystal perpendicular to c-axis [46].

The synthesis and the conductivities of Ti-doped apatite-type phases of the composition of $(La/Ba)_{10-x}(Si/Ge)_6O_{26+z}$, where Ti substituted at the Si/Ge site, were reported by Sansom et al [47]. The conductivities were shown to be the highest for the samples containing either cation vacancies or oxygen excess, which is consistent with previous studies of apatite-type oxide ion conductors. However, the Ti doping was shown to generally decrease the conductivity in comparison with equivalent samples containing only Si/Ge at the tetrahedral sites, with the greatest decrease for Si-containing samples.

Vanadium-doped oxyapatite phases of the composition of $La_{10-x}V_x(SiO_4)_6O_{3+x}$ were prepared by Yuan et al [48] via the sol-gel method. The apatite phase begins to form at 800°C, which is much lower than in the case of conventional solid-state synthesis method. The best conductivity of $La_9V(SiO_4)_6O_4$ is $1.67 \cdot 10^{-2}$ S·cm^{-1}, which is significantly higher than that for lanthanum silicate oxides ($1.19 \cdot 10^{-2}$ S·cm^{-1}). The valence ion V^{5+} doped for La^{3+} does lead to the formation of hexagonal apatites even with high oxygen contents.

The phase $La_5Si_2BO_{13}$ [49],[50],[51] crystallizes with apatite-related structure (**Fig. 4**) with the space group $P6_3/M$ and the cell parameters ***a*** = 9.5587 Å, ***c*** =7.2173 Å and ***Z*** = 2. The composition of these apatite-like compounds can be also expressed via the general formula: $La_{9.33+x}Si_{6-2y}B_{3y}O_6$, where $0 \le x \le 0.67$. At limiting compositions x = 0.67, La(2) site is fully occupied, and the formula referred to the unit cell is $La_{10}Si_4B_2O_{26}$ or, more simply, $La_5Si_2BO_{13}$.

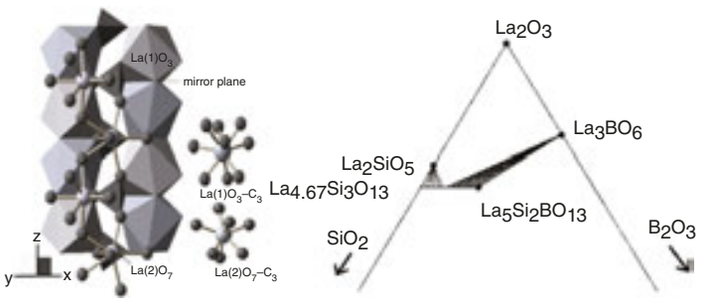

Fig. 4. The crystal structure of $La_5Si_2BO_{13}$ (a) [51] and the upper section of the ternary phase diagram La_2O_3-SiO_2-B_2O_3 at 1100°C (b) [49].

The comparison with other apatite-like structures shows lower distortion in the M(1) polyhedron and unusually short bond length from La in the M(2) site and O(4) oxygen in the column site (2.303 Å). These results can be explained in view of the presence of trivalent La and divalent O, respectively, in the M(1) and M(2) sites and in the column anion site, whereas, in apatites, these sites are occupied by divalent and monovalent ions, respectively [49].

The preparation of La-Si-O apatite-type thin films was described by Vieira et al [52] with Si/(La + Si) atomic ratios ranging from 0.36 to 0.43 being produced via the magnetron sputtering in reactive Ar/O discharge gas. The apatite-type lanthanum silicate phase was formed in all as-deposited films upon the annealing at 900°C for 1 h. The lanthanum silicate films obtained by annealing the as-deposited films with lower Si/(La + Si) atomic ratios have a preferential orientation with the c-axis perpendicular to the substrate, while low-intensity diffraction peaks ascribed to $La_2Si_2O_7$ phase were detected in the films deposited with higher

Si content. Preferentially oriented films have higher activation energy and lower ionic conductivity, as the ionic conductivity measurements were performed in the direction perpendicular to the c-axis. The highest ionic conductivity was obtained for the film deposited with a Si/(La + Si) atomic ratio of 0.42, with a value of 1.2×10^{-2} S·cm^{-1} at 750°C. By the incorporation of oxygen in the as-deposited films, the silicon segregation upon annealing was avoided.

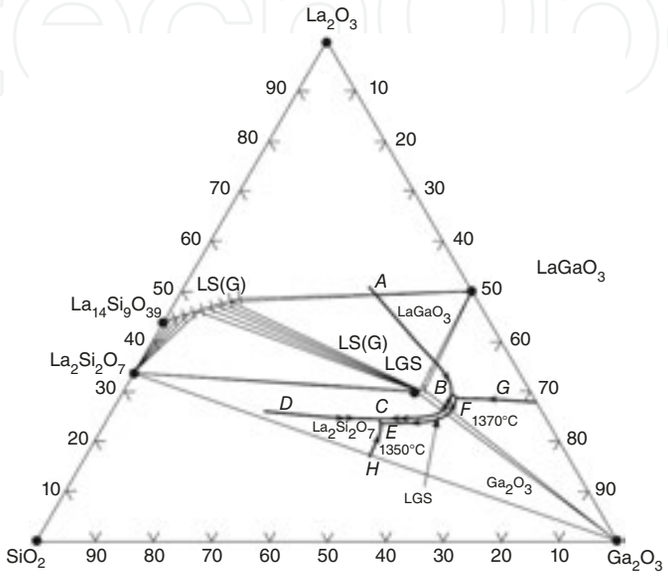

Fig. 5. Primary phase diagram of ternary system La_2O_3-Ga_2O_3-SiO_2 around LGS [53].

The formation of ternary compound with apatite structure in the system La_2O_3-Ga_2O_3-SiO_2 (**Fig. 5**) was first reported by Wang and Uda [53]. The apatite phase, which precipitates from the melt of the composition around that of stoichiometric $La_3Ga_5SiO_{14}$ (LGS), can be described by the formula: $La_{14}Ga_xSi_{9-x}O_{39-x/2}$, where $0 \leq x \leq 3.5$. Since there is a large field for the formation of solid solutions with the range extending from $La_{14}Si_9O_{39}$ to Ga_2O_3, some Si^{4+} sites are probably substituted by Ga^{3+}.

The liquidus surface of LS(G) was determined to be the field on the Ga_2O_3-poor side of boundary curve ABCD. The liquidus surface of LS(G) covers the stoichiometric composition of LGS. In this field, the crystallization of LS(G) aciculae was observed in all samples that were heated to temperatures above 1500°C. The liquidus volume of LGS is denoted by the field BCEF. It seems to be a narrow field in the composition between the liquidus surfaces of LS(G) and Ga_2O_3. E and F are eutectic points, where LGS + $LaGaO_3$ + Ga_2O_3 + liquid and LGS + Ga_2O_3 + $La_2Si_2O_7$ + liquid were found, respectively [53].

The CaO-La_2O_3-SiO_2-P_2O_5 phase diagram was investigated by El Ouenzerfi et al [54] in order to determine a domain inside which all points correspond to pure apatitic oxyphosphosilicates with the general formula: $Ca_xLa_y(SiO_4)_{6-u}(PO_4)_uO_t$. The defined domain (**Fig. 6**) is only a part of the whole existence domain of the apatitic structure, but it allows to prepare pure apatitic samples with well-controlled composition.

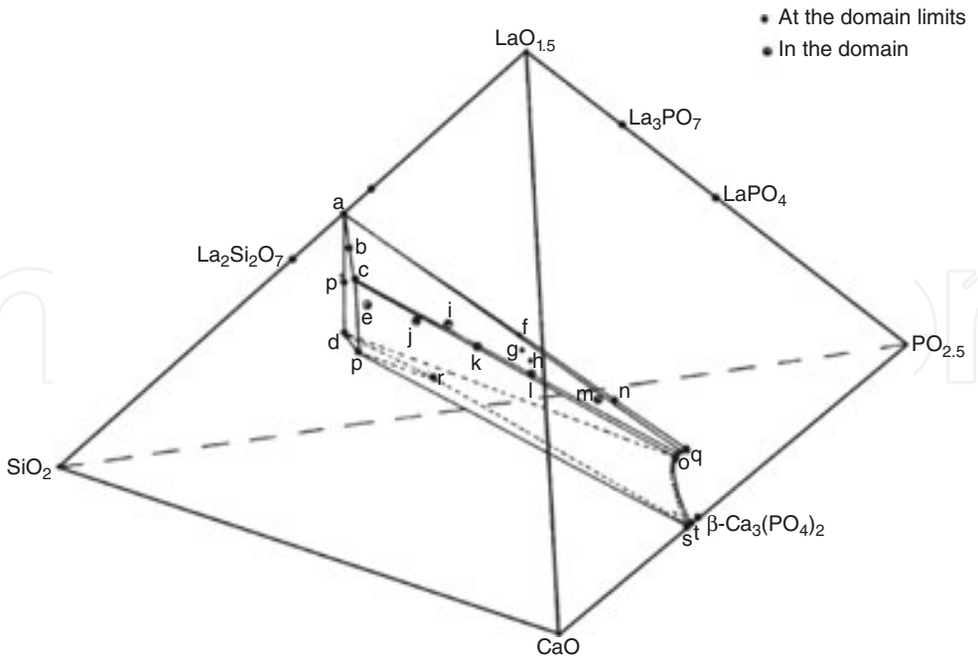

Fig. 6. Britholite stability domain in the CaO-SiO_2-La_2O_3-P_2O_5 quaternary system [54].

For these samples, the continuous change of the stoichiometry of each element proves that it exists as a solid solution including the oxygen content. This observation completes the literature data where britholites are presented as limited to three series corresponding to the stoichiometry [54],[55]:

1. $Sr_{2+x}La_{8-x}(SiO_4)_{6-x}(PO_4)_xO_2$ with $0 \le x \le 6$ [13];

2. $Sr_{3+x}La_{6-x}(SiO_4)_{6-x}(PO_4)_x$ with $0 \le x \le 1.5$;

3. $Sr_{4+x}La_{6-x}(SiO_4)_{6-x}(PO_4)_xO$ with $0 \le x \le 6$.

Inside this domain, the solid solution continuously varies between pure phosphate apatites $Ca_xLa_y(PO_4)_6O_t$ and pure silicate apatites $Ca_xLa_y(SiO_4)_6O_t$ and also between oxyapatites $Ca_xLa_y(SiO_4)_{6-u}(PO_4)_uO_t$ and nonoxyapatites $Ca_xLa_y(SiO_4)_{6-u}(PO_4)_u$.

During the investigation of the kinetics of solid-state sintering[14] of strontium-doped apatite-type lanthanum silicates ($Sr_xLa_{10-x}Si_6O_{27-x/2}$) under isothermal conditions (1250 – 1550°C), Bonhomme et al [56] recognized that the densification mechanism of the apatite ceramics was

[13] Wanmaker et al [55] reported the synthesis of apatite-type compounds of the composition:

(a) $M^{2+}(II)M(III)_{8-x}(SiO_4)_{6-x}(PO_4)_xO_2$, where $0 \le x \le 6$;

(b) $M(II)_{3+x}M(III)_{6-x}(SiO_4)_{6-x}(PO_4)_x$, where $0 \le x \le 1.4$;

(c) $M(II)_{4+x}M(III)_{6-x}(SiO_4)_{6-x}(PO_4)_xO$, where $0 \le x \le 6$.

where M(II) = Ca, Sr, Ba, Mg, Zn or Cd and M(III) Y or La. The paper also contains structural data for several other newly prepared oxy-britholites, including $Zn_2La_8(SiO_4)_6O_2$, $BaMgY_8(SiO_4)_6O_2$, $Zn_2Y_8(SiO_4)_6O_2$, $Cd_2Y_8(SiO_4)_6O_2$, $Ca_4La_5(SiO_4)_5(PO_4)$ and $Ba_4La_5(SiO_4)_5(PO_4)$.

http://dx.doi.org/10.5772/62209

controlled by the diffusion of rare-earth element (La) at the grain boundaries. This process showed the activation energy of 470 kJ·mol^{-1}.

The ternary phase diagram Al_2O_3-SiO_2-La_2O_3 at 1300°C (**Fig. 7**) was investigated by Mazza and Ronchetti [57]. $La_{14}Si_9O_{39}$ was described by Kuz'min and Belov [58] as an apatite-like structure of hexagonal symmetry (space group $P6_3/m$). Isomorphous compounds were also reported for Nd [59], Ce [60] and Sm [58]. The $La_{14}Si_9O_{39}$ compound extends its stability range in the interior of the phase diagram, forming the solid solution of the type $La_{14+1x/3}Si_{9-x}Al_xO_{39}$, which is stable from $x = 0$ to $x = 1.5$. This substitution stoichiometry (Al + 1/3La ↔ Si) can be described as a tetrahedral Al for Si substitution on the 6*h* position and contemporary occupation of vacant La sites [57].

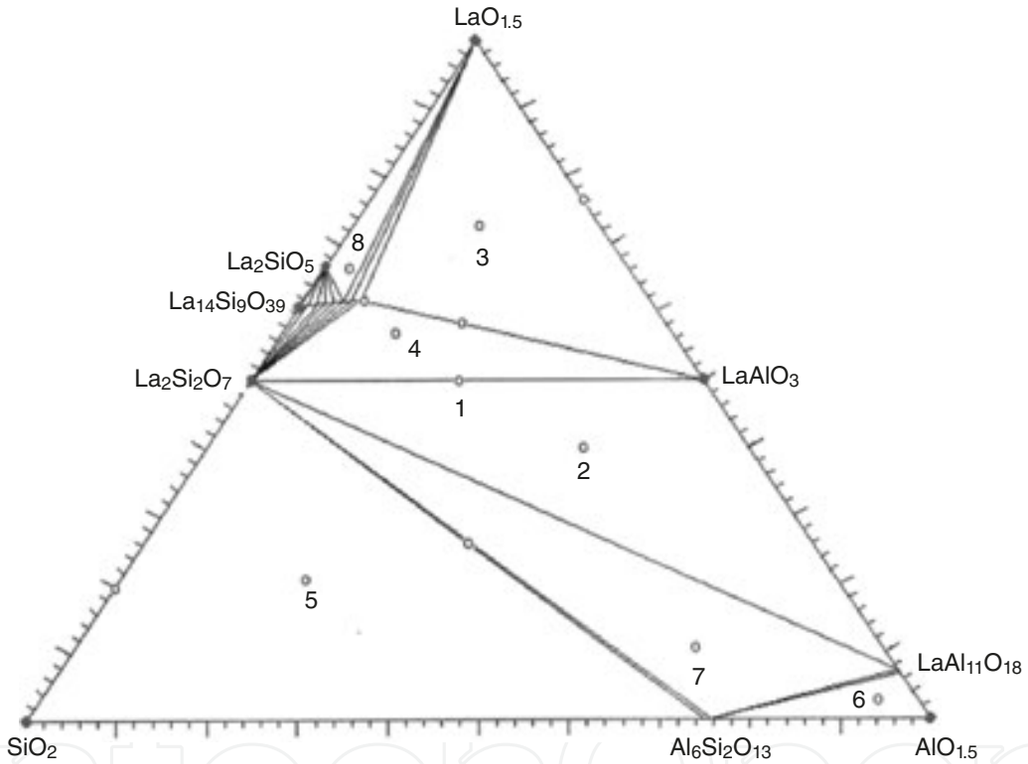

Fig. 7. Ternary phase diagram at 1300°C in air [57].

[14] The densification rate is considered as the function of temperature (***T***) and mean grain size (D_m). Constant ***A*** depends on the surface energy (γ_{sg}) of grains, on the apatite molar volume (Ω) and on average coefficient of diffusion of limiting species ***D***. This relationship can be written as follows [56]:

(a) $\frac{d\rho}{dt} = \frac{AD}{T D_m^n}$

The coefficient of diffusion ***D*** is thermally activated:

(b) $D = D_0 \exp\left(-\frac{E_a}{RT}\right)$

where D_0 is the pre-exponential coefficient of diffusion, ***R*** is the universal gas constant and E_a is the apparent activation energy of diffusion of the rate limiting process. Exponent ***n*** in **Eq. (a)** depends on the mechanism of transport of the limiting species governing the kinetics of densification.

5.2 Apatite-type lanthanium germanates

Lanthanum germanate and silicate apatite-based materials, both undoped and with partial substitution of, for example, Al, B instead of Si and Sr in place of La, are promising oxide ion conductors with potential applications as high-temperature solid electrolytes. Considerable uncertainties remain over the stoichiometry, the defect structure and the conductivity variations within various apatite systems, partly caused by the fact that the La:(Ge, Si) ratio is variable, giving rise to the solid solutions in the undoped systems as well as to the solid solutions formed by partial replacement of La and/or (Si, Ge) together with, depending on the solid solution mechanism, variations in oxygen content [24].

The preparation of single crystal of apatite-type lanthanium germanate of the composition of $La_{9.33}Ge_6O_{26}$ was reported by Nakayama and Sakamoto [61]. The mixtures of La_2O_3 and GeO_2 were well mixed in ethanol under an atomic ratio of La:Ge = 9.33:6 using a ball mill. The mixture was dried and then calcined in air at 1000°C for 2 h. The resulting $La_{9.33}Ge_6O_{26}$ powders were further ball milled into finer powders. After the pre-sintering, the closely packed $La_{9.33}Ge_6O_{26}$ powders were heated at 1300°C for 2 h in air, and the surface of the specimen was mirror polished. The polished surface of polycrystalline $La_{9.33}Ge_6O_{26}$ ceramics was then bonded to a <001> face of $La_{9.33}Ge_6O_{26}$ seed crystal prepared by the Czochralsky (**Section 4.2**) method. On heating of the bonded sample at 1525 – 1550°C, continuous grain growth of polycrystalline $La_{9.33}Ge_6O_{26}$ occurred and the single crystal was gradually grown from the seed crystal into the polycrystalline region [61].

Apatite-type lanthanium germanate possesses hexagonal structure with the space group $P6_3/m$ and the lattice parameters: a = 9.9256 and c = 7.2900 Å, $\boldsymbol{V}$ = 621.97 Å^3 and $\boldsymbol{Z}$ = 2. The calculated density of the phase is 2.148 g·cm^{-3}. Similar to apatite-type lanthanium silicate ($La_{9.33}Si_6O_{26}$) described above, the structure of $La_{9.33}Ge_6O_{26}$ (**Fig. 8**) contains two different sites for atoms of La. The La(1) and La(2) sites are located at 4*f* and 6*h*, respectively. While the $La_{9.33}Ge_6O_{26}$ single crystal showed little anisotropy in conductivity, the conductivity of $La_{9.33}Si_6O_{26}$ single crystal gave 100 times higher value parallel to the c-axis than that perpendicular to the c-axis at each temperature (**Section 5.1**) [61].

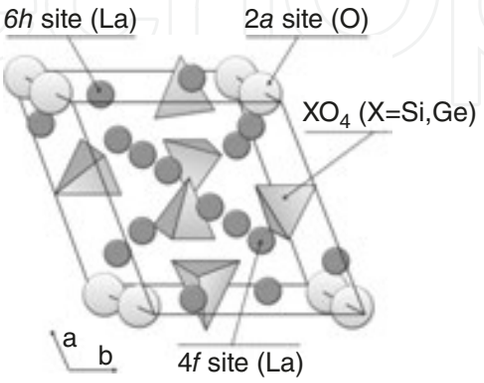

Fig. 8. Hexagonal structure proposed for the apatite-type phase of $La_{9.33}X_6O_{26}$, where X = Si and Ge [61].

The selective doping of $La_{9.33+x}(GeO_4)_6O_{2+3x/2}$ with Y leads to the stabilization of hexagonal lattice, even at high oxygen contents. Furthermore, this has the effect of enhancing the low-temperature conductivities [62]. Depending on the composition, the cell can be either hexagonal or triclinic, with the evidence of reduced low-temperature conductivities for the latter, attributed to increased defect trapping in this lower symmetry cell. In summary, it was shown that the series $La_8Y_2(GeO_4)_{6-x}(GaO_4)_xO_{3-x/2}$ can be prepared for $0 \le x \le 2$ with all samples showing the hexagonal symmetry, compared to the series without Y co-doping, $La_{10}(GeO_4)_{6-x}(GaO_4)_xO_{3-x/2}$, for which all compositions display the triclinic symmetry [24],[62], [63].

The effect of Ga doping of the oxygen stoichiometric series containing the cation vacancies, $La_{7.33+y/3}Y_2(GeO_4)_{6-y}(GaO_4)_yO_2$ ($0 \le y \le 2$), single-phase samples was obtained for $y \ge 1.0$, with small impurities observed at lower Ga contents. The conductivities were shown to increase with increasing cation vacancy content, reaching the values of ≈0.02 $S \cdot cm^{-1}$ at 800°C, which are similar to the oxygen excess series. These results are in agreement with previous reports on the apatite systems, which showed that the oxide ion conductivity was maximized in samples containing the oxygen excess and/or the cation vacancies [24], [62],[63].

The series of apatite-type silicates/germanates of the composition of $La_{8+x}Sr_{2-x}Si_6O_{26+x/2}$ ($0 \le x \le 1$) and $La_{8+x}Sr_{2-x}Ge_6O_{26+x/2}$ ($0 \le x \le 2$) were prepared from high-purity La_2O_3, $SrCO_3$, SiO_2 and GeO_2 by Orera et al [64] via the thermal treatment of these components mixed in the stoichiometric ratio.

The extent of, and the structural changes within, the apatite domain in the $LaO_{1.5}$-GeO_2-SrO ternary system at 1100°C was studied and the single-phase samples were obtained for $La_{9.33+x-2y/3}Sr_y(GeO_4)_6O_{2+1.5x}$ with x = 0.17 and 0.34. The hexagonal to triclinic transition is clearly associated with increasing oxygen content rather than with filling the La sites by the addition/substitution of Sr into the structure. The limits of undoped solid solution are ~$0.17 \le x \le 0.5$ at 1100°C [24].

The hydrothermal synthesis of apatite-type compound $NaRE_9(GeO_4)_6O_2$ (RE = Nd, Pr) with the hexagonal structure of the space group of $P6_3/M$ was described by Emirdag-Eanes et al [65]. The structure is composed of REO_7 and REO_9 polyhedra as well as GeO_4 tetrahedra (**Fig. 10**). The unit cell dimensions are: a = 9.782(1) Å, c = 7.083(1)Å (T = 293 K) and V = 587.0(2)Å3 for REE = Nd and a = 9.802(1) Å, c = 7.116(1)Å (T = 293 K) and V = 592.1(2)Å3 for REE = Pr.

The high-temperature flux method for the preparation of single crystal of hexagonal $NaLa_9Ge_6O_{26}$ apatite-type germanate (space group $P6_3/M$, $\boldsymbol{a}$ = 9.883, $\boldsymbol{c}$ = 7.267 Å and $\boldsymbol{Z}$ = 1) was used by Takahashi et al [66]. The crystal structure (**Fig. 11**) was found to be similar to that of silicate oxyapatite $NaY_9Si_6O_{26}$. The 4*f* cation sites are occupied disorderedly by La and Na. On the other hand, the 6*h* cation sites are occupied by La only. This compound constitutes a new member of the oxyapatite-type structure family with the composition given by general formula: $A_xLn_{10-x}B_6O_{24}O_{3-x}$.

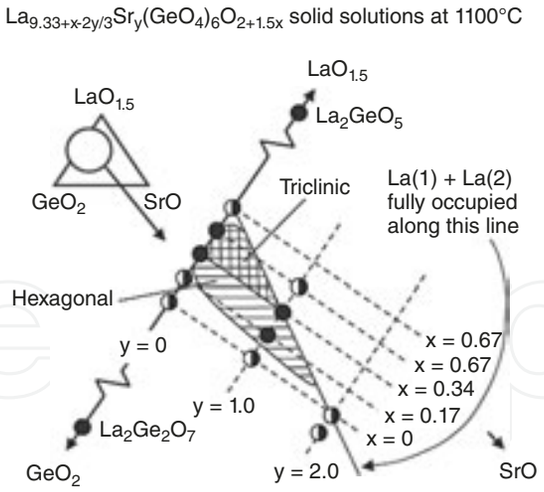

Fig. 9. Apatite solid solutions in the $LaO_{1.5}$-GeO_2-SrO ternary system [24]: pure phases are indicated by filled circles and the presence of secondary phases is shown by half-filled circles.

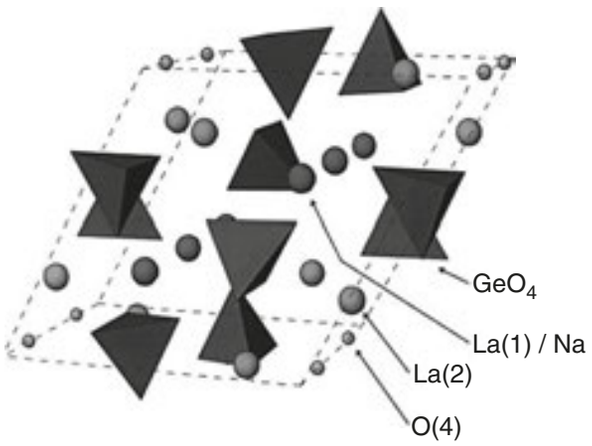

Fig. 11. The structure of sodium lanthanum germanate $NaLa_9Ge_6O_{26}$ [66].

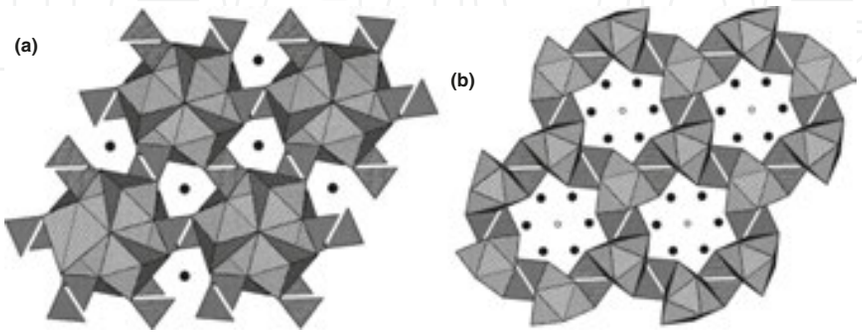

Fig. 10. The unit cell view with GeO_4 and NdO_7 (a) and GeO_4 and NdO_9 down the c-axis. NdO_7 and NdO_9 are dotted polyhedra, and GeO_4 are lined polyhedra [65].

http://dx.doi.org/10.5772/62209

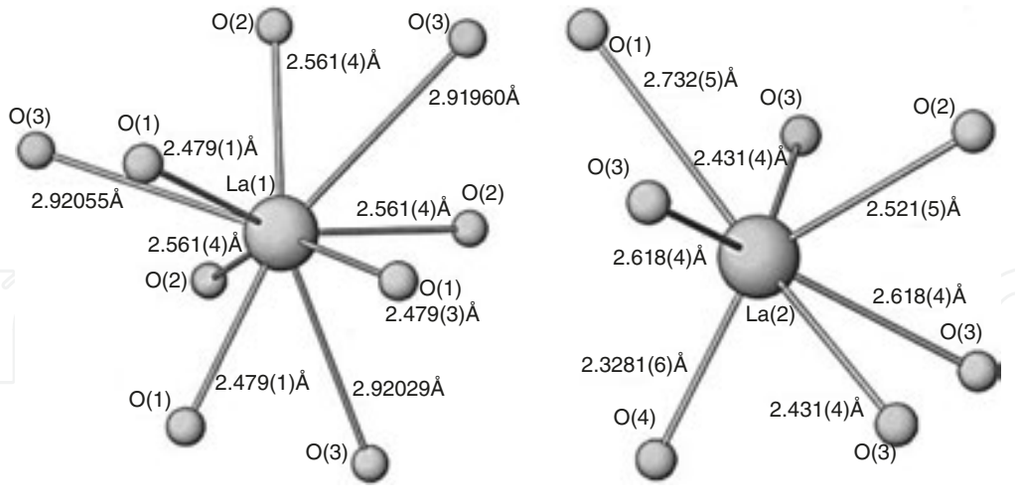

Fig. 12. Coordination environment of La atoms [66].

The coordination environments of La atoms by O atoms are shown in **Fig. 12**. La(1) atom on the 4*f* site is coordinated by nine O atoms. It is linked to three O(1) atoms in a distance of about 0.2479 nm, to three O(2) atoms in a distance of about 0.2561 nm and to three O(3) atoms in a distance of about 0.2924 nm. Because the distance between La(1) and O(3) is relatively large, La(1) atom can be also regarded to be in sixfold coordination, the environment of which is fairly distorted from an ideal octahedron. On the other hand, La(2) atom, which occupies the 6h position, is coordinated by seven O atoms, that is, O(1), O(2), O(4) and O(3). The distances of those two types of bonds between La(2) and O(3) atoms are 0.2618 nm×2 and 0.2431 nm×2, respectively. Those between La(2) and O(1), O(2) and O(4) are 0.2732, 0.2521 and 0.23281 nm, respectively [66].

5.3 Apatite-type borates

Two high terbium content apatites $Tb_5Si_2BO_{13}$ (a = 9.2569 Å, c = 6.8297 Å, $\boldsymbol{V}$ = 506.83 Å^3 and $\boldsymbol{Z}$ = 2) and $Tb_{4.66}Si_3O_{13}$ (a = 9.493 Å, c = 6.852 Å, $\boldsymbol{V}$ = 534.70 Å^3 and $\boldsymbol{Z}$ = 2) were prepared by Chen and Li [67] via spontaneous crystallization and synthesized with high purities and excellent crystallinities by the sol-gel process. Both compounds are isostructural with $P6_3/M$ space group and exhibit paramagnetic behavior down to 2 K. Owing to high Tb^{3+} ion concentrations and good transmittance in the range from 500 to 1500 nm, $Tb_5Si_2BO_{13}$ and $Tb_{4.66}Si_3O_{13}$ may be promising magneto-optical materials in the visible-near-IR range.

Both $Tb_5Si_2BO_{13}$ and $Tb_{4.66}Si_3O_{13}$ contain two distinct sites for Tb^{3+} cations, which are depicted in **Fig. 13**. Tb(2) is at the 4*f* site, which is on a threefold axis and coordinated by nine oxygen ions. However, for $Tb_{4.66}Si_3O_{13}$, the Tb(2) site is not fully occupied but leaves one of six Tb(2) positions randomly vacant while fully occupied in $Tb_5Si_2BO_{13}$. In contrast, Tb(1) at the 6*h* site is fully occupied and sevenfold coordinated in both $Tb_5Si_2BO_{13}$ and $Tb_{4.66}Si_3O_{13}$. Moreover, in $Tb_5Si_2BO_{13}$, one third of Si is disorderly occupied by B, which gives rise to extra 1/3 Tb^{3+} ion for the charge balance. The $Tb(2)O_9$ polyhedron consists of Tb(2) and nine oxygens along the c-

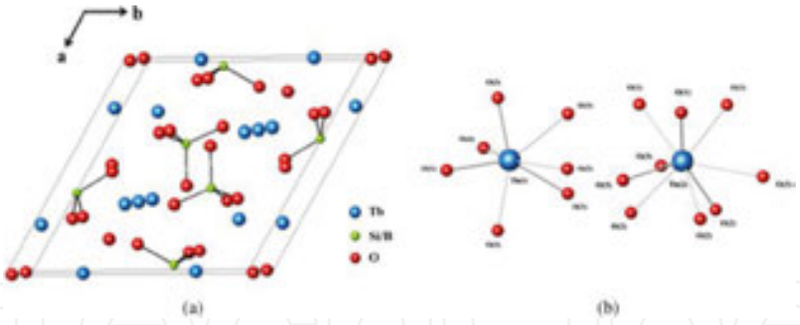

Fig. 13. Unit cell of $Tb_5Si_2BO_{13}$ (a) and coordination environment of kinds of Tb cations (b) [67].

axis. Six Tb(1) comprise a sixfold channel parallel to the c-axis. It is worth to note that the channel is considered to play an extremely important role in oxide ion conductivity [67].

The structure and optical properties of noncentrosymmetric borate $RbSr_4(BO_3)_3$ (RSBO) was described by Xia and Li [68]. RSBO can be viewed as a derivative of the apatite-like structure. Based on the anionic group approximation, the optical properties of the compound are compared to those of the structure-related apatite-like compounds with the formula "$A_5(TO_n)_3X$". When the structures of all apatite-like crystals are presented in orthorhombic unit cell, the arrangements of planar anionic BO_3 groups are all similar to one-third of the BO_3 groups aligned perfectly parallel at corner- and face-centered locations, whereas the other two-thirds of BO_3 groups are distributed differently.

Europium borate fluoride, $Eu_5(BO_3)_3F$ with an apatite-type structure, was synthesized by Kazmierczak and Höppe [69] as single-phase crystalline powder starting from europium oxide, europium fluoride and boron oxide at 1370 K. $Eu_5(BO_3)_3F$ crystallizes in the space group Pnma.

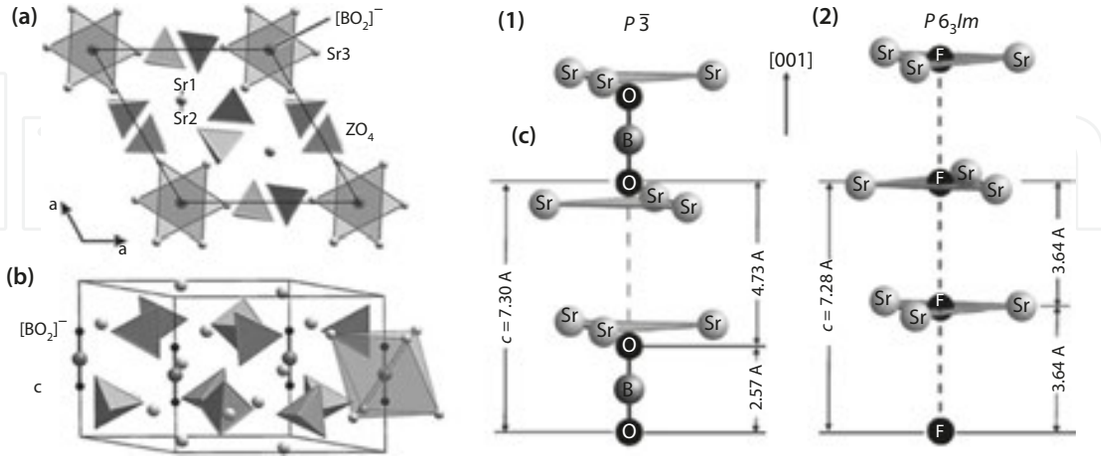

Fig. 14. The crystal structure of $Sr_{10}[(PO_4)_{5.5}(BO_4)_{0.5}](BO_2)$ (1): (a) the projection along [001] showing the channels formed by Sr3 (gray triangles) and the positions of the XO_4 tetrahedra (gray; Z = 11/12 P + 1/12B) and (b) the side view with emphasized $[BO_2]^-$ groups and the coordinating trigonal antiprism formed by Sr3. The comparison of the arrangement of $[BO_2]^-$ and F- ions within the Sr channels of $Sr_{10}(PO_4)_{5.5}(BO_4)_{0.5}(BO_2)$ (c(1)) and $Sr_{10}(PO_4)_6F_2$ (c(2)) [70].

The structure of single crystal of strontium phosphate orthoborate metaborate ($Sr_{10}[(PO_4)_{5.5}(BO_4)_{0.5}](BO_2)$) that was grown from the melt by Chen et al [70] is shown in **Fig. 14**(a). The phase crystallizes in the space group P3 with the cell parameters ***a*** = 9.7973 Å, ***c*** = 7.3056 Å, ***V*** = 607.19 Å^3 and ***Z*** = 1. The crystal structure is closely related to apatite and contains linear metaborate groups, $[BO_2]^-$ (point group $D_{\infty h}$, B-O = 1.284 Å), taking positions within the channels running along the threefold inversion axis. Strontium sites are found to be fully occupied, while $[PO_4]^{3-}$ tetrahedra are partially replaced by$[BO_4]^{5-}$ groups.

The comparison of the nearest neighbors around $[BO_2]^-$ and F^- located within the channels is shown in **Fig. 14**(**b**,**c**). F^- ions (0,0,1/4) are situated on the mirror plane in the center of Sr triangle. As a result, constant F…F distances of 3.64 Å (***a***/2) are observed along [001] (**b**). In $Sr_{10}[(PO_4)_{5.5}(BO_4)_{0.5}](BO_2)$, the incorporation of boron atoms between two O atoms draws these atoms closer (d(O-B-O) = 2.57 Å) and at the same time increases the gaps between two neighboring $[BO_2]^-$ units (d(O…O) = 4.73 Å), which results in alternating O…O distances along the c-axis (**a**) [70].

By replacing Mn in $YCa_3(MnO)_3(BO_3)_4$ with trivalent Al and Ga, two new borates with the compositions of $YCa_3(MO)_3(BO_3)_4$ (M = Al, Ga) were prepared via the solid-state reaction by Yu et al [71]. The phases are isostructural to gaudefroyite with the hexagonal space group $P6_3/m$. The cell parameters of ***a*** = 10.38775 Å, ***c*** = 5.69198Å for the Al-containing compound and ***a*** = 10:5167 Å, ***c*** = 5:8146 Å for the Ga analogue were obtained from the refinements. The structure is constituted of AlO_6 or GaO_6 octahedral chains interconnected by BO_3 groups in the ***ab*** plane to form a Kagomé-type lattice[15] [72],[73],[74], leaving trigonal and apatite-like tunnels. It was found that most rare-earth and Cr, Mn ions can be substituted into the Y^{3+} and M^{3+} sites, respectively, and the preference of rare-earth ions to be located in the trigonal tunnel is correlated to the sizes of the M^{3+} ions.

5.4 Other apatite-type REE silicates

Hexagonal apatite-type phase of the composition of $Pr_9K(SiO_4)_6O_2$ (space group $P6_3/m$, a = 9.6466 Å and c = 1136 Å, V = 573.28 Å^3, ρ_{calc} = 5.48 g·cm^{-3} and Z = 1) was synthesized by Werner and Kubel [75] in a potassium fluoride flux. Potassium fills one (4*f*) of two metal positions present in the structure (**Fig. 15**) with the occupancy factor of 25%. The remaining positions of this site (Pr2/K2) are occupied by praseodymium.

[15] The Kagomé lattice (**d**) is one of the most interesting lattices in 2D, especially in materials in which the Kagome lattice is built from magnetic ions. Each of its vertices touches a triangle, hexagon, triangle and hexagon (the planes of corner-sharing equilateral triangles). The vertices correspond to the edges of the hexagonal (honeycomb) lattice (**c**), which in turn is the dual of triangular lattice (can be derived from triangular lattice by periodical removal of ¼ sites) (**b**). Since it has the same coordination number (z = 4), the Kagomé lattice is also related to the square lattice (**a**) [72], [73]. Numerous Kagomé compounds built from stacked Kagomé layers were found in Alunite (Jarosite, $KFe^{3+}{}_3(SO_4)_2(OH)_6$, (**e**)) family of minerals [74].

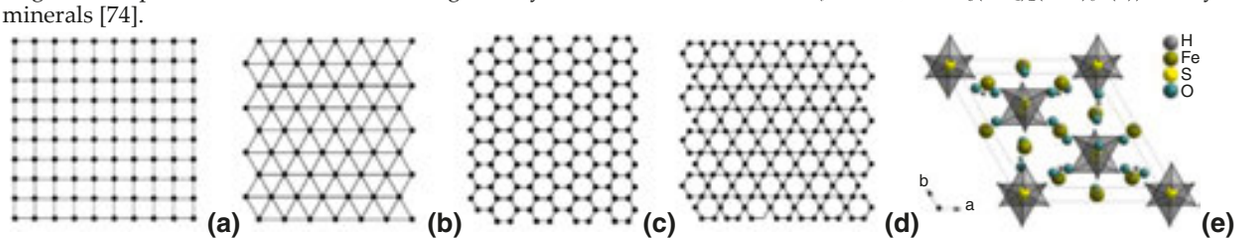

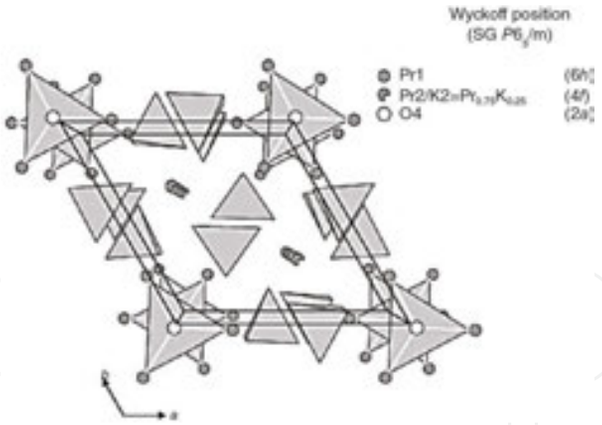

Fig. 15. The perspective view of $Pr_9K(SiO_4)_6O_2$ along the c-axis: regular planar coordination of the channel oxygen O(4) and the SiO_4 tetrahedra are marked in gray, and the unit cell is outlined [75].

Oxygen from the silicate groups forms a coordination polyhedron (ninefold) in the shape of a distorted threefold capped trigonal prism. These face sharing [(Pr2/K2)O_9]-polyhedra build up chains, which are interconnected via the SiO_4 groups. The resulting channel framework accommodates sevenfold oxygen-coordinated praseodymium (Pr1), attached to the inside of the tubes that are aligned parallel to the c-axis. Oxide ions O4, located on the longitudinal axis of the channels, exhibit anomalously high atomic displacement parameters along the c-direction [75].

Single crystals of apatite-type $Nd_{9.33}(SiO_4)_6O_2$, $Pr_{9.33}(SiO_4)_6O_2$ and $Sm_{9.33}(SiO_4)_6O_2$ were described in **Section 4.2.2**. The structure of samarium orthosilicate oxyapatite ($Sm_5(SiO_4)_3O$, **Fig. 16**) was resolved by Morgan et al [76]. The phase crystallizes in hexagonal system with the space group $P6_3/M$ and the cell parameters: $\boldsymbol{a}$ = 9.4959 Å, $\boldsymbol{c}$ = 7.0361 Å, $\boldsymbol{c}$:$\boldsymbol{a}$ = 0.7410 and $\boldsymbol{V}$ = 549.46 Å^3. The preparation and the structure of single crystal of strontium tetrapraseodymium tris(silicate) oxide ($SrPr_4(SiO_4)_3O$), which was grown by the self-flux method using $SrCl_2$, was described by Sakakura et al [77].

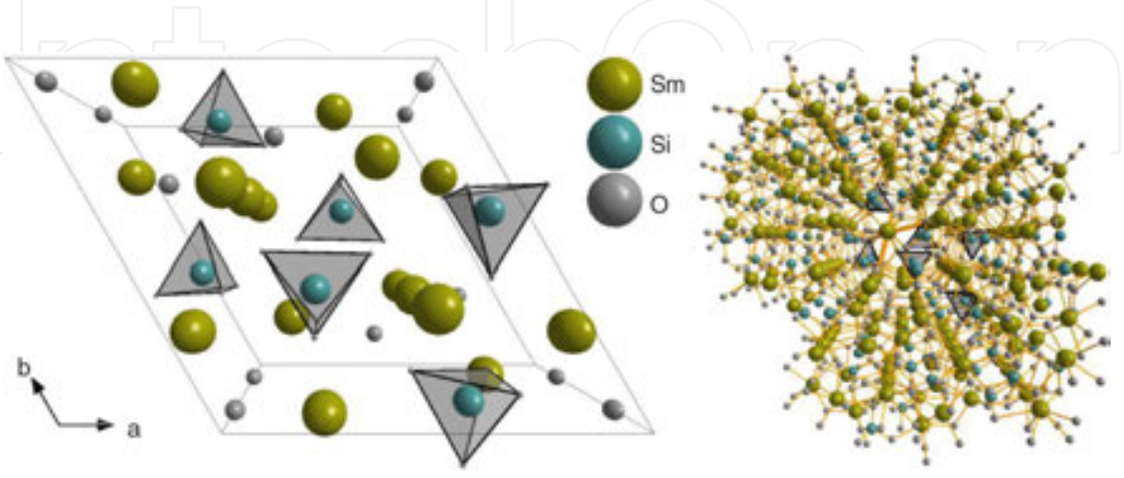

Fig. 16. The structure of $Sm_5(SiO_4)_3O$ viewed along the c-axis [76].

The M(2) sites are almost exclusively occupied by praseodymium. The complete series of apatite-like compounds $REE_{9.33}\square_{0.67}[SiO_4]_6O_2$, $LiREE_9[SiO_4]_6O_2$ and $NaREE_9[SiO_4]_6O_2$ were synthesized by Felsche [78] with REE: La → Lu. Apatite-type neodymium silicates doped with various cations at the Si site, $Nd_{10}Si_5BO_{27-\delta}$ (B = Mg, Al, Fe, Si), were synthesized by Xiang et al [79] via the solid-state reaction.

The crystal growth and the structure of three new neodymium-containing silicates, $Na_{0.50}Nd_{4.50}(SiO_4)_3O$, $Na_{0.63}Nd_{4.37}(SiO_4)_3O_{0.74}F_{0.26}$ and $Na_{4.74}Nd_{4.26}(O_{0.52}F_{0.48})[SiO_4]_4$, prepared using the eutectic mixture of KF/NaF were investigated by Latshaw et al [80]. $Na_{0.50}Nd_{4.50}(SiO_4)_3O$ and $Na_{0.63}Nd_{4.37}(SiO_4)_3O_{0.74}F_{0.26}$ adopt the apatite structure and crystallize in hexagonal space group $P6_3/M$, while $Na_{4.74}Nd_{4.26}(O_{0.52}F_{0.48})[SiO_4]_4$ crystallizes in tetragonal space group I-4 and exhibits rare-earth mixing on the sodium site. The unit cell parameters of the crystals are:

1. $Na_{0.50}Nd_{4.50}(SiO_4)_3O$: a = 9.5400 Å and c = 7.033 Å;
2. $Na_{0.63}Nd_{4.37}(SiO_4)_3O_{0.74}F_{0.26}$: a = 9.5533 Å and c = 7.0510 Å;
3. $Na_{4.74}Nd_{4.26}(O_{0.52}F_{0.48})[SiO_4]_4$: a = 12.1255 Å and c = 5.4656 Å.

Double REE silicate $Gd_{4.33}Ho_{4.33}(SiO_4)_6(OH)_2$ with the hydroxylapatite structure was synthesized by Wang et al [81] using the piston-cylinder high-pressure apparatus at the pressure of 2.0 GPa and the temperature of 1450°C. Since they have nearly identical chemical character, two REE cations (Ho and Gd) are distributed randomly among the M(1) and M(2) sites, and the charge balance is maintained by the cation vacancies in M(1). The presence of two different REE cations in the same compound might promote better understanding of the cooperative effects of ions under the solid-state conditions (**Fig. 17**).

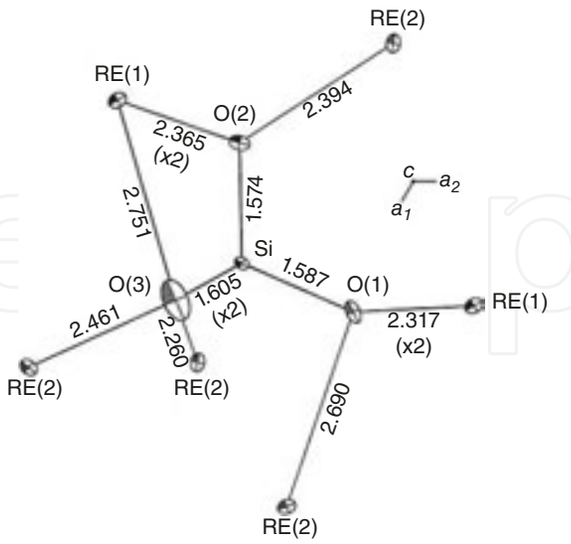

Fig. 17. Bond distances (Å) and anisotropic displacement in $Gd_{4.33}Ho_{4.33}(SiO_4)_6(OH)_2$: note that the exaggerated anisotropic displacement of O(3) is attributable to the high proportion of vacancies in REE(1) and near-equatorial distribution of strong bonds to Si and REE(2) [81].

The structure analysis reveals that the hexagonal compound crystallizes in usual apatite space group $P6_3/M$ with lattice parameters ***a*** = 9.3142 Å and ***c*** = 6.7010 Å. REE(1) atoms are connected to nine oxygen atoms with the REE(1)-O bond distances ranging from 2.317 to 2.751 Å (mean 2.478 Å) and REE(2) atoms are connected to seven oxygen atoms with the RE(2)-O bond distances ranging from 2.223 to 2.690 Å (mean 2.393 Å). Oxygen anion O(4) in the apatite channel is located on the 6_3 axis and coordinated with three REE(2) cations arranged in a tricluster perpendicular to the c-axis. An isotropic displacement parameter was used for O(4), and H atom was assumed to ride on it. OH^- anions are stacked in regular column in the apatite channel, and in locally ordered structure, their polar direction is flipped in neighboring channel [81].

The formation of apatite-type phases of the composition of $KNd_6(SiO_4)_6O_2$ from the glass precursor ($4K_2O$-Nd_2O_3-$17SiO_2$) during the hydrothermal experiments (500°C and 825 bar) carried out at KOH molarities of 6 or greater was reported by Haile et al [82]. High temperatures, high pressures and long times tended to favor the synthesis of this apatite-type phase over the $K_8Nd_3Si_{12}O_{32}OH$ phase. In comparison with the potassium system, the concentration of NaOH required for the synthesis of $NaNd_6(SiO_4)_6O_2$ phase (system $4Na_2O$-M_2O_3-$17SiO_2$, where M = Nd and Y) is very low. The formation of apatite-type phases in the $4Na_2O$-Y_2O_3-$17SiO_2$ system was not observed [83].

Two series of strontium-lanthanum apatites, $Sr_{10-x}La_x(PO_4)_{6-x}(SiO_4)_xF_2$ and $Sr_{10-x}La_x(PO_4)_{6-x}(SiO_4)_xO$ with $0 \le x \le 6$, were synthesized by Boughzala et al [84] via the solid-state reaction in the temperature range of 1200 – 1400°C:

$$\begin{aligned} &3\ SrCO_3 + (6-x)/2\ Sr_2P_2O_7 + SrF_2 + x\ SiO_2 + x\ La(OH)_3 \rightarrow \\ &Sr_{10-x}La_x(PO_4)_{6-x}(SiO_4)_xF_2 + 3\ CO_2 + 3x/2\ H_2O \end{aligned} \tag{9}$$

and

$$\begin{aligned} &4\ SrCO_3 + (6-x)/2\ Sr_2P_2O_7 + x\ SiO_2 + x\ La(OH)_3 \rightarrow \\ &Sr_{10-x}La_x(PO_4)_{6-x}(SiO_4)_xO + 4\ CO_2 + 3x/2\ H_2O \end{aligned} \tag{10}$$

where x = 0, 1, 2, 4 and 6. $Sr_2P_2O_7$ was synthesized by the following reaction at 900°C:

$$2\ SrCO_3 + 2\ (NH_4)_2HPO_4 \rightarrow Sr_2P_2O_7 + 2\ CO_2 + 3\ H_2O + 4\ NH_3 \tag{11}$$

The raw meal was prepared via mixing $SrCO_3$, La_2O_3, SiO_2, SrF_2 and $(NH_4)_2HPO_4$ in required stoichiometric amounts ($0 \le x \le 6$). The mixture was ground in an agate mortar, pressed to pellets and calcined at the temperature of 900°C for 12 h under the flow of argon ($Sr_{10-x}La_x(PO_4)_{6-x}(SiO_4)_xF_2$) and oxygen ($Sr_{10-x}La_x(PO_4)_{6-x}(SiO_4)_xO$). The product was ground and pressed again in order to improve its homogeneity. Next, thermal treatment was performed

http://dx.doi.org/10.5772/62209

at the temperature of 1200 and 1400°C (depending on the content of SiO_2) for 12 h. The samples were heated and cooled with the rate of 10°C·min^{-1}. The incorporation of La^{3+} and SiO_4^{4-} ions into the apatite structures, i.e. the substitution of the pair La^{3+} and SiO_4^{4-} for Sr^{2+} and PO_4^{3-}, induced an increase of parameter ***a*** and decrease of parameter ***c*** (**Fig. 18**) [84].

The formation of nanocrystalline Ce-Yb mixed silicate-type oxyapatite of the composition of $Yb_yCe_{9.33-y}(SiO_4)_6O_2$ via the solid-state synthesis was described by Małecka and Kępiński [85]. The phase was identified as an intermediate formed during the synthesis of Ce-Yb silicates.

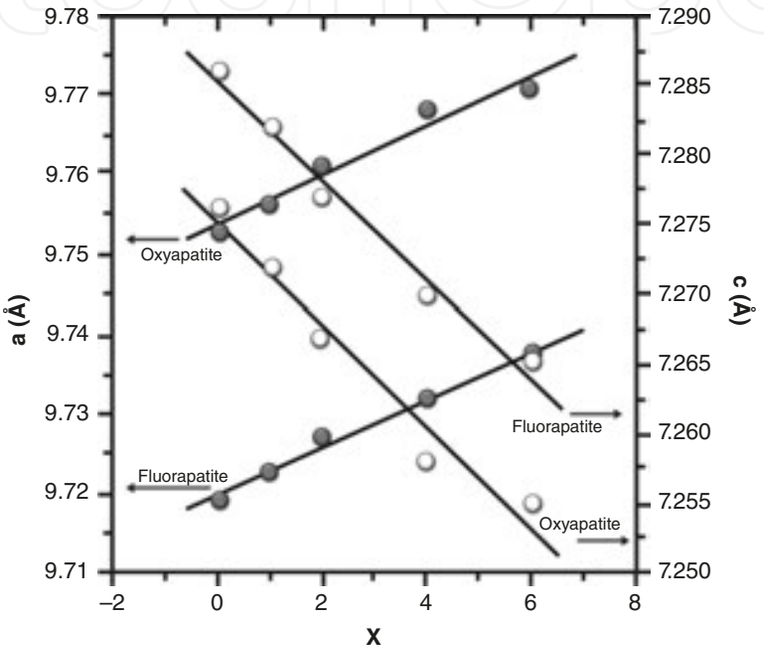

Fig. 18. The variation of *a* and *c* parameters of $Sr_{10-x}La_x(PO_4)_{6-x}(SiO_4)_xF_2$ and $Sr_{10-x}La_x(PO_4)_{6-x}(SiO_4)_xO$ phases with the value of *x* [84].

Different compositions of apatite-type $La_{10}Si_{6-x}W_xO_{27+\delta}$ ceramics were prepared successfully by Xiang et al [86] via the high-temperature solid-state reaction route. Doping with W^{6+} is beneficial to the removal of La_2SiO_5 impurity phase. When the doping content of W^{6+} is more than 0.1, the rod-like grains of $La_{10}Si_{6-x}W_xO_{27+\delta}$ ceramics are replaced gradually by equiaxed apatite-type grains, and randomly shaped convex $La_6W_2O_{15}$ particles appear at the grain boundaries. While doping with Nb^{5+} leads to the hexagonal-phase $La_{9.5}Ge_{5.5}Nb_{0.5}O_{26.5}$, the addition of MO^{6+} leads to the compound $La_{9.5}Ge_{5.5}Mo_{0.5}O_{26.75}$ with triclinic symmetry [87].

5.5 Apatite-type yttrium silicates

5.5.1 Yttrium silicates

The formation of the phase with the composition ($Y_4Si_3O_{12}$, $Y_4(SiO_4)_3$ or $2Y_2O_3{\cdot}3SiO_2$ [88]), which is stable between 1650 and 1950°C, was reported by Toropov and Bondar [89] in the binary system of Y_2O_3-SiO_2 and by Toporov and Fedorov [90] in the ternary system of CaO-Y_2O_3-SiO_2

(**Fig. 19**(**a**)). This was the first reported occurrence of the phase with the composition between yttrium orthosilicate (Y_2SiO_5, oxyorthodsilicate, YSO, Y_2O_3:SiO_2 = 1:1 [91]) and yttrium disilicate $Y_2Si_2O_7$ (yttrium pyrosilicate, YPS, 1:3). The structure of this phase was described as the garnet type [88].

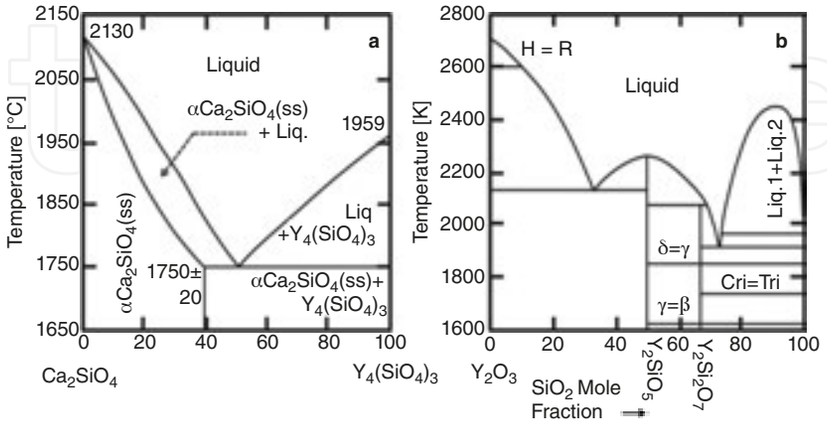

Fig. 19. Phase equilibrium in the system Ca_2SiO_4-$Y_4(SiO_4)_3$ according to Toporov and Fedorov [90] and Y_2O_3-SiO_2 phase diagram [92].

Since then, authors have disagreed about the existence of such a phase because the attempts to make it starting with yttria and silica powders resulted in the formation of only Y_2SiO_5 and $Y_2Si_2O_7$ [93]. This phase was not reported either by other studies of Y_2O_3-SiO_2 system [92],[94], [95], which contains two compounds. Y_2SiO_5 and$Y_2Si_2O_7$ were found, with two (A and B) and five (*y*, α, β, γ and δ, also called *y*, B, C, D and E [96]) polymorphs, respectively. The first has a congruent melting, whereas the second has an incongruent one (**Fig. 19**(**b**)).

Nevertheless, the formation of oxyapatite phase of the composition of $Y_{4.67}\square_{0.33}(SiO_4)_3O$ (7:9) prepared via the oxidation of nitrogen apatite $Y_5(SiO_4)_3N$ was reported by other authors [7], [97]. The apatite-like phase $Y_{4.67}(SiO_4)_3O$ possesses hexagonal structure with the space group $P6_3/M$, a = 9.368 and c = 6.735 Å [78],[98]. The specific gravity of the phase is 4.39 g·cm^{-3} and the hardness on the Mohs scale is 5 – 7 [99].

Since the structure of YSO containing two different types of anions includes the $[SiO_4]^{4-}$ complex ion and an additional non-silicon-bonded oxygen ion (NBO), it could be written as $Y_2(SiO_4)O$. This compound also displays two structure types of monoclinic symmetry with different linking of O-Y_4 tetrahedra. Low-temperature X_1 phase and high-temperature X_2 phase belong to the space groups of $P2_1/C$ (Z = 2) and $C2/C$ (Z = 8), respectively [91].

The samples of the composition of $Y_4(SiO_4)_3$, and similar ones containing small amount of iron oxide, corresponding to an overall composition of $Fe_{0.2}Y_4(SiO_4)_3O_{0.2}$, were produced by the mixed powder method and by the sol-gel route using yttrium nitrate ($Y(NO_3)_3{\cdot}5H_2O$), TEOS (tetraethylorthosilicate) and iron nitrate ($Fe(NO_3)_3{\cdot}9H_2O$) by Parmentier et al [7]. Nitrate was dissolved in ethanol/water mixture (volume ratio 7:3), the amount of the latter being controlled to give final Si concentration. Iron nitrate was added at this stage in calculated amounts corresponding to the final iron-doped apatite composition. The solution was stirred for a few

http://dx.doi.org/10.5772/62209

hours and TEOS was added to give the appropriate silicon content and then the solution was placed in an oven at 60°C until the gelation occurred. The gel was dried at 80°C and calcined at 600°C for 1 h.

Powders prepared by the two routes were uniaxially pressed into pellets and treated to temperatures up to 1650°C in air in a Pt crucible, or for the heat treatments at 1700°C, carbon element furnace was used, and the samples were heated in a BN-lined crucible in nitrogen atmosphere. Iron appears to have two roles depending on the temperature; it stabilizes the apatite phase at high temperatures when produced by the sol-gel route and catalyzes the decomposition of sol-gel-derived apatite at low temperatures [7].

A new phase of yttrium magnesium silicate having the apatite structure was prepared by Suwa et al [100] at 1500°C in air. Its chemical composition can vary from $(Y_4Mg)Si_3O_{13}$ to $(Y_{4.33}Mg_{1.13})Si_{3.34}O_{13}$. The hexagonal unit cell dimensions $\boldsymbol{a}_0$ and $\boldsymbol{c}_0$ of $(Y_4Mg)Si_3O_{13}$ are 9.298 ± 0.002A and 6.635 ± 0.001A, respectively, and its axial ratio c/a is 0.714. It is optically uniaxial negative with $\varepsilon = 1.810 \pm 0.005$, $\omega = 1.820 \pm 0.005$ and $\omega - \varepsilon = 0.010$. The cleavages parallel and perpendicular to the c-axis were recognized. The formation of the apatite-type phase of the composition of $NaY_9Si_6O_{26}$ in the ternary system Na_2O-Y_2O_3-SiO_2 was also reported by Lee et al [101].

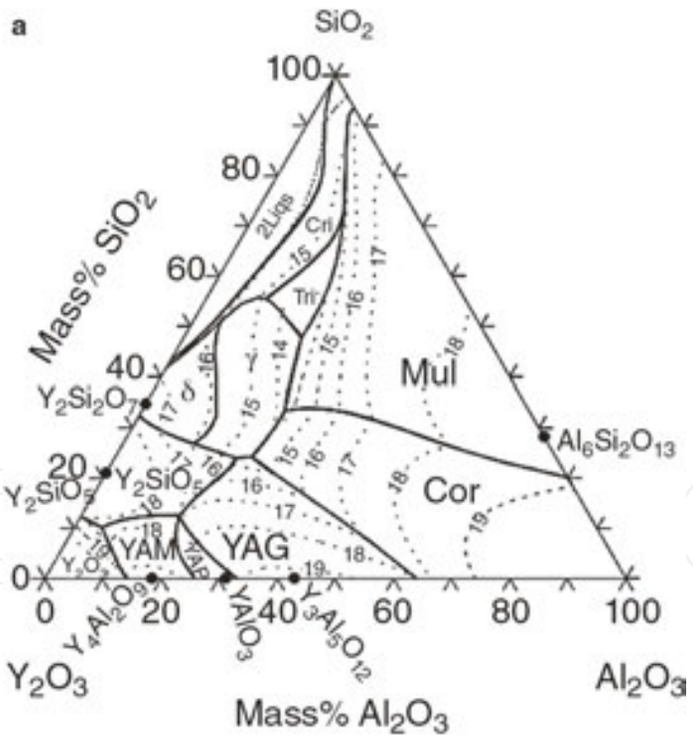

Fig. 20. Calculated liquidus surface of the Y_2O_3-Al_2O_3-SiO_2 system: three-phase equilibria with liquid phase (thick lines), liquidus surfaces for various solids (labeled area) and isothermal section (dotted lines, temperature in hundreds °C) [92].

The phase diagram of Al_2O_3-SiO_2-La_2O_3 system (**Fig. 20**) can be compared with the Y_2O_3-Al_2O_3-SiO_2 ternary diagram examined by Bondar and Galakhov in 1964 [102]. The latter represents

the only other example of REE_2O_3-Al_2O_3-SiO_2 phase diagram found so far in the literature. The authors identified the liquidus surface of the whole ternary field, but they failed to elucidate the subsolidus phase relationships among different binary compounds. Due to the much smaller ionic size of Y^{3+} ion with respect to La^{3+} ion (1.18 and 1.015 Å for the eightfold coordination, respectively [103]) and lower bond-valence parameter (2.019 and 2.172 Å [104]), the stability of the binary compositions is substantially altered [57].

The β-alumina-like phase $LaAl_{11}O_{18}$ is no longer stable, while the garnet-like phase $Y_3Al_5O_{18}$ and $Y_4Al_2O_9$ monoclinic compound exist. The lacunar apatite-like phase $Y_{14}Si_9O_{39}$ reported by Wills et al [105] does not appear in the Y_2O_3-Al_2O_3-SiO_2 ternary diagram; however, a compound with similar Y/Si atomic ratio, namely $Y_4Si_3O_{12}$, also reported by Wills et al [105], does. Since the formation of $Y_4Si_3O_{12}$ phase was not confirmed, it may be stabilized by impurities [57],[92].

5.5.2 AM and AEE-yttrium orthosilicate oxyapatites

Alkaline metals (AM) and alkaline-earth element oxyapatites (oxybritholites) are described in this chapter. Phosphate minerals of the apatite supergroup possess strong affinity for strontium [106]. The apatite-type phase of the composition of $Sr_2Y_8Si_6O_{26}$ ($Sr_2Y_8(SiO_4)_6O_2$) was prepared by Zuev et al [107] via the two-stage calcination of mixture of $SrCO_3$, Y_2O_3, Eu_2O_3 and SiO_2 in air in order to investigate the spectral characteristics of $Sr_2Y_8(SiO_4)_6O_2$:Eu polycrystals. The structure of apatite phase is shown in **Fig. 21**. The sol-gel synthesis and the characterization of $Sr_2Y_{8(1-x)}Eu_{8x}Si_6O_{26}$ solid solution doped by Eu, where x = 0.01 – 0.4, was described by Karpov and Zuev [108]. The formation of calcium analogue ($Ca_2Y_8(SiO_4)_6O_2$, calcium-yttrium-silicate oxyapatite) was observed during the crystallization of SiO_2-Al_2O_3-CaO-Na_2O-K_2O-F-Y_2O_3 glass ceramics [109] and during the degradation of advanced environmental barrier coatings [110]. The phase $Ca_4Y_6(SiO_4)_6O_2$ was often prepared in order to investigate its luminescent properties [111],[112].

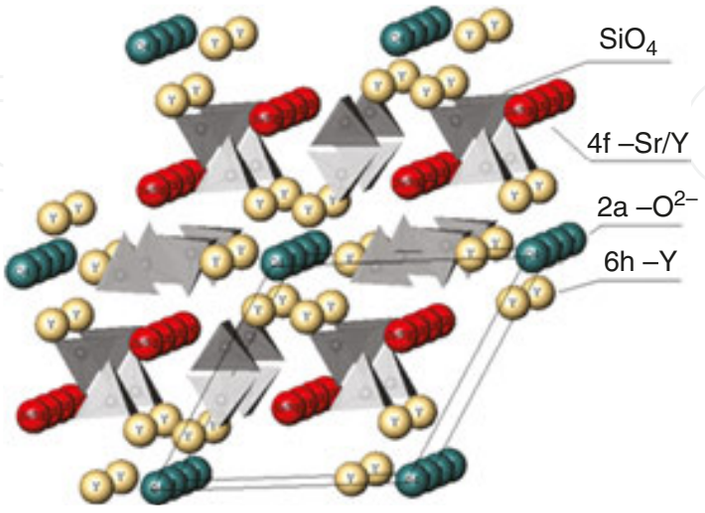

Fig. 21. The structure of $Sr_2Y_8(SiO_4)_6O_2$ [107].

http://dx.doi.org/10.5772/62209

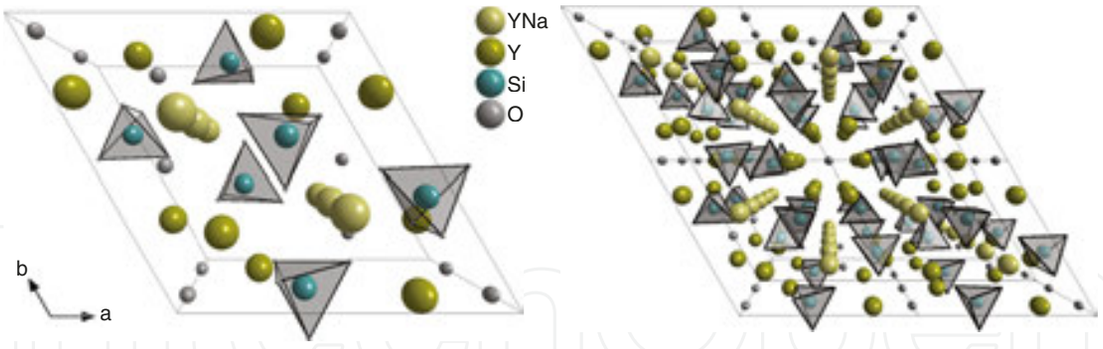

Fig. 22. The structure of $NaY_9(SiO_4)_6O_2$ oxyapatite (the perspective view along the c-axis) [114].

The precipitation of $NaY_9(SiO_4)_6O_2$ apatite-type compound (sodium nonayttrium hexakis(silicate) dioxide) in the SiO_2-B_2O_3-Al_2O_3-Y_2O_3-CaO-Na_2O-K_2O-F glass-ceramics system (**Section 10.3.8**) was described by VAN'T HOEN et al [113]. The hexagonal structure of $NaY_9(SiO_4)_6O_2$ oxyapatite (**Fig. 22**) was resolved by GUNAWARDANE et al [114]. The phase crystallizes in $P6_3/M$ space group with the cell parameters ***a*** = 9.334, ***c*** = 6.759 Å, ***c***:***a*** = 0.7241, *V* = 509.97 Å and ***Z*** = 1).

Lithium yttrium orthosilicate ($LiY_9(SiO_4)_6O_2$, lithium nonayttrium hexakis(silicate) dioxide) crystallizes in centrosymmetric space group $P6_3/M$. The structure closely resembles those of fluorine apatite. There are two different crystallographic sites for Y^{3+} ion, which are coordinated by seven and nine O atoms. One-fourth of the nine-coordinated site is occupied by Li atoms, thus maintaining the charge balance. Si atom occupies the tetrahedral site [115].

The preparation, the properties and the effect of sintering additives of hexagonal ($P6_3/M$) strontium-yttrate-silicate oxyapatite (oxybritholite2) with the composition of $SrY_4(SiO_4)_3O$ as the main product of sinter-crystallization process, in which the non-equilibrium melt was formed in the temperature interval from 1300 to 1550°C in the SrO-Y_2O_3-SiO_2 system, was described by PTÁČEK et al [116]. The formation of non-equilibrium melt is facilitated by borate fluxes, alkaline fluxes and talc. The apparent activation energy and the frequency factor of the sinter-crystallization process were determined to be 1525 kJ mol^{-1} and $1.04 \cdot 10^{45}$ s^{-1}, respectively. The material shows low value of linear thermal expansion coefficient of $(1.1 \pm 0.1) \cdot 10^{-6}°C^{-1}$ in the temperature range from 25 to 850°C.

The course of synthesis can be expressed by the following reaction formula [116]:

$$AEECO_3 + 2\ Y_2O_3 + 3\ SiO_2 \rightarrow AEE\ Y_4[SiO_4]_3O + CO_2(g) \qquad (12)$$

This **reaction 12** is too general to describe formed intermediates ($SrSiO_3$, Sr_2SiO_4, SrY_2O_4, …[16]) and the process of sinter-crystallization of apatite:

[16] Detailed description of formed intermediates can be found in work [116].

$$\begin{aligned} &AEECO_3 + 2\ Y_2O_3 + 3\ SiO_2 \rightarrow \text{int ermediates} \rightarrow \\ &\text{non} - \text{equilibrium melt} \rightarrow AEE\ Y_4\left[SiO_4\right]_3 O + CO_2(g) \end{aligned} \tag{13}$$

Since the formation of $SrY_4(SiO_4)_3O$ proceeds thorough non-equilibrium melt phase, the effect of sintering additives such as borate fluxes, fluorides and carbonates of alkaline metals as well as talc was investigated. Sintering additives facilitate the formation of melt phase and increase the length of sinter-crystallization interval. The expansion after the thermal decomposition of strontium carbonate is reduced as well. Calcinate, treated to the temperature lower than the temperatures of sinter-crystallization interval, has hydraulic activity. Therefore, it can be applied in special composite cements as an activator for latent hydraulic and pozzolanic materials.

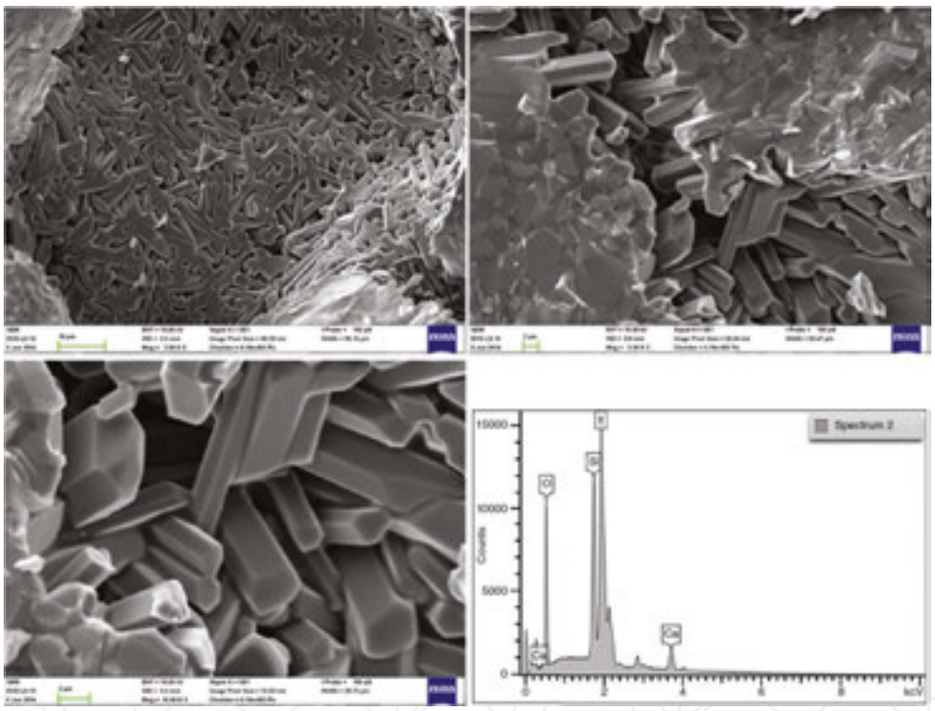

Fig. 23. SEM picture and WDX analysis of hexagonal crystal of $CaY_4(SiO_4)_3O$ apatite phase.

Effect on sinter-crystallization process	Decreasing intensity or temperature of effect →
Expansion before sinter-crystallization	Pure >> NaF >> Talc ≈ Li_2CO_3 ≈ $Li_2B_4O_7$ >> Na_2CO_3 > $LiBO_2$ > K_2CO_3
Firing shrinkage (sample treated to 1600°C)	$LiBO_2$ > $Li_2B_4O_7$ ≈ Pure > NaF > K_2CO_3 ≈ Na_2CO_3 > Talc > Li_2CO_3
Initial temperature of sinter-crystallization	Pure ≈ Na_2CO_3 ≈ Talc > $Li_2B_4O_7$ > K_2CO_3 ≈ NaF > $LiBO_2$ > Li_2CO_3
Maximum rate of sinter-crystallization	Li_2CO_3 > Pure > Li_2B4O_7 ≈ Talc ≈ NaF ≈ K_2CO_3 ≈ Na_2CO_3 > $LiBO_2$
Length of interval of sinter-crystallization	$LiBO_2$ >> $Li_2B_4O_7$ ≈ NaF > Li_2CO_3 > pure > Talc > Na_2CO_3 > K_2CO_3

Table 3. The influence of sintering additive on the behavior during thermal treatment [116].

After the process of sinter-crystallization, the reactivity of glassy phase with water drops. A significant benefit of talc is the fact that the glassy phase surrounding the crystals of apatite phase becomes resistant against the influence of water with this sintering additive. Furthermore, magnesium is not being incorporated into the structure of apatite phase during the crystallization of $SrY_4(SiO_4)_3O$ from non-equilibrium melt. The influence of sintering additives on the behavior during the thermal treatment is summarized in **Table 3** [116].

The important feature of this compound is the formation of colored center after the exposition to X-ray radiation (**Fig. 24**); hence, the prepared material is an important candidate for optical applications, sensors and dosimeters.

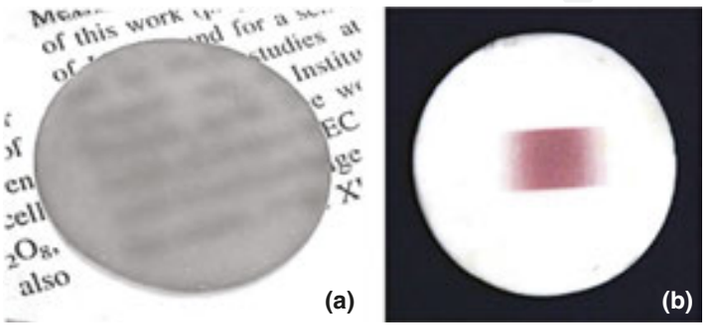

Fig. 24. Semitransparent disc of $SrY_4(SiO_3)_4O$ sintered specimen (a) and formation of colored center on X-ray irradiated area (Cu(Ka), 40 kV and 30 mA) [116].

On the other hand, this reaction also indicates that the synthesis of individual apatite analogues ($AEEY_4(SiO_4)_3O$, where AEE = Ca, Sr and Ba) and their solid solutions proceeds via similar ical intermediates formed in the temperature range, which is affected by the thermal stability of AEE carbonates that increases in the order: $CaCO_3$, $SrCO_3$ and $BaCO_3$.

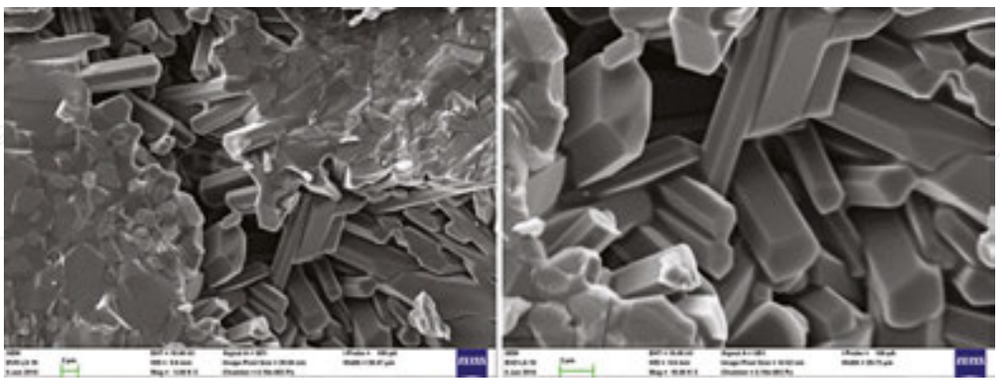

Fig. 25. SEM picture of hexagonal crystal of $CaY_4[SiO_4]_3O$ apatite phase.

While the synthesis of $CaY_4(SiO_4)_3O$ leads to well-developed hexagonal crystals (**Fig. 25**), the attempts for the preparation of $BaY_4(SiO_4)_3O$ phase were not successful. This synthesis leads to well-developed crystals of yttrium orthosilicate (Y_2SiO_5) surrounded by $BaO\text{-}Y_2O_3\text{-}SiO_2$ glassy phase (**Fig. 26**).

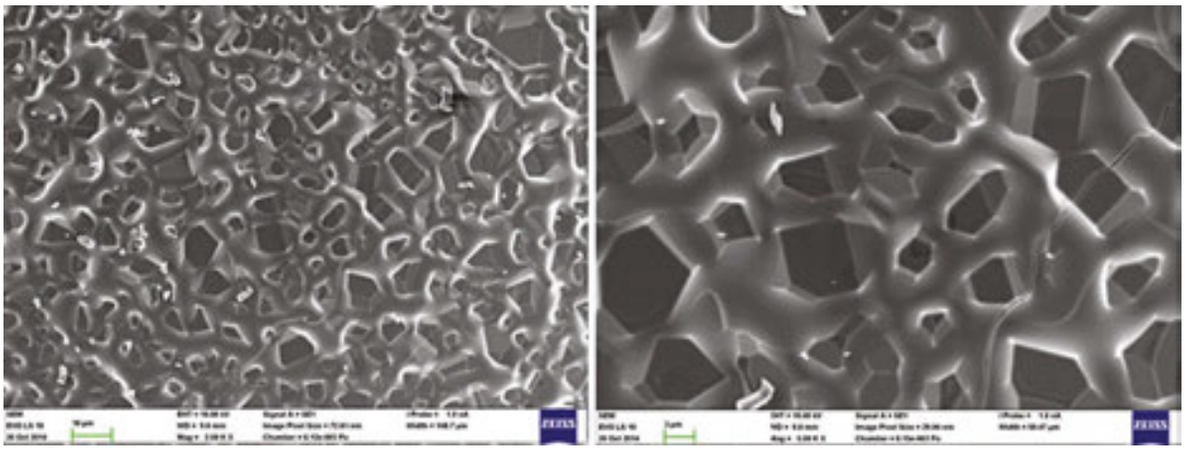

Fig. 26. SEM of Y_2SiO_5 crystal surrounded by barium-containing glassy phase.

The investigation of this system leads to the conclusion that non-limited $Ca^{2+} \leftrightarrow Sr^{2+}$ substitution can be performed in the binary system of $(Ca\text{-}Sr)Y_4[SiO_4]_3O$. On the contrary, the $BaY_4[SiO_4]_3O$ analogue of $CaY_4[SiO_4]_3O$ and $SrY_4[SiO_4]_3O$ apatite cannot be prepared; therefore, the extent of $Ca^{2+} \leftrightarrow Ba^{2+}$ and $Sr^{2+} \leftrightarrow Ba^{2+}$ substitutions is limited to 28 ± 4 and 38 ± 4%, respectively. The field of ternary solid solutions in the $AEEY_4[SiO_4]_3O$ system, where AEE = Ca, Sr and Ba, is shown in **Fig. 27**.

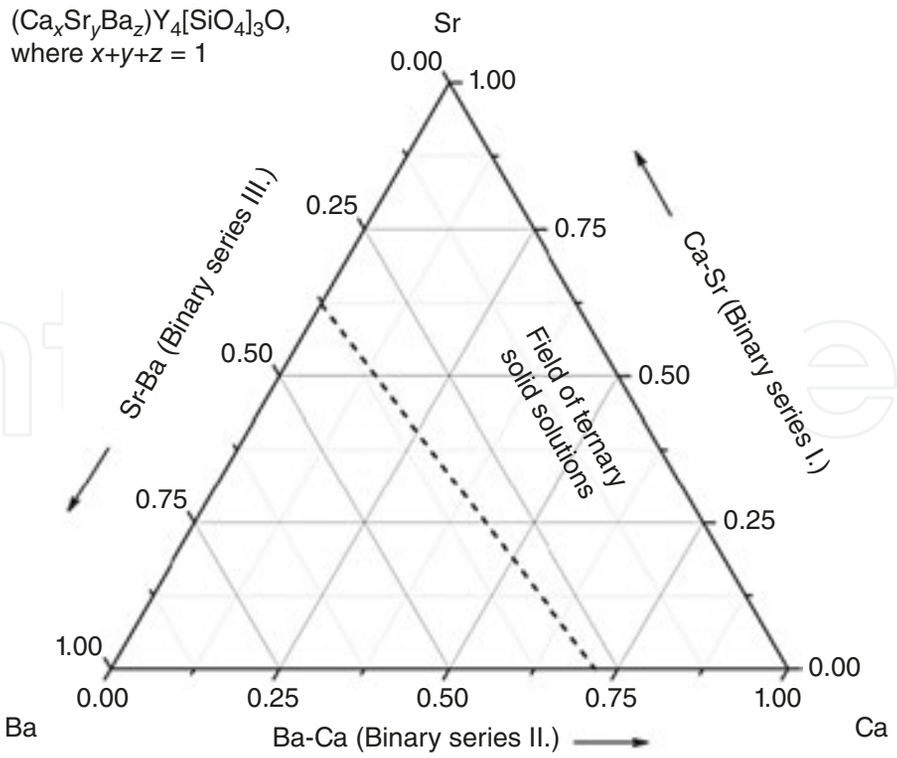

Fig. 27. The miscibility in the AEE $Y_4(SiO_4)_3O$ system.

5.5.3. N-apatite

The main secondary phases in Jänecke prism[17] [117] for Si_3N_4-Al_2O_3-SiO_2-Y_2O_3-YN-AlN system[18] are shown in **Fig. 28**. The formal exchange of oxygen by nitrogen leads to the compounds of N-apatite ($Y_{10}(SiO_4)_6N_2$, H-phase[19]), N-melilite[20] [118] ($Y_2Si_3O_3N_4$, M-phase), N-wollastonite ($YSiON_2$, K-phase) and N-woehlerite ($Y_4Si_2O_7N_2$, J-phase). The latter one forms a complete solid solution with $Y_4Al_2O_9$ (YAM) of the composition of $Y_4Si_{2-x}Al_xO_{7+x}N_{2-x}$ (Jss-phase) [119],[120], [121],[122],[123],[124].

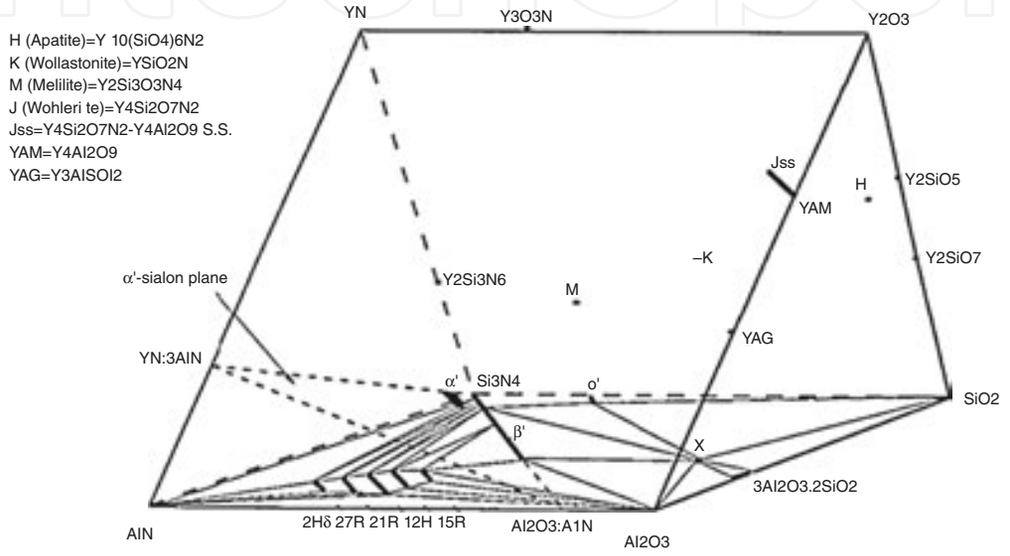

Fig. 28. Representation of the Si_3N_4-Al_2O_3-SiO_2-Y_2O_3-YN-AlN phase equilibrium.

$Y_{10}(SiO_4)_6N_2$ (N-apatite, H-phase, $(Y,Si,\square)_{10}[Si(O,N)_4]_6(O,N,\square)_2$ [125], silicon-yttrium oxynitride) was first identified by Rae et al [126] as a compound with the compositional mixture of $10Y_2O_3{\cdot}9SiO_2{\cdot}Si_3N_4$ that was stable up to 1750°C. There were other suggested compositions, such as $Y_{10}Si_7O_{23}N_4$ [127]. Later work by Gauckler et al [128] established N-apatite as a stoichiometric compound with the formula unit of $Y_{10}[SiO_4]_6N_2$ and the apatite structure (space group $P6_3/M$). The lattice constants of the hexagonal cell were reported to be ***a*** = 9.638

[17] Jänecke prism is used to visualize the phase relationships among α-sialon, β-sialon and other phases in the M-Si-Al-O-N system. α- and β-sialons are isostructural with α- and β-Si_3N_4, respectively. The substitution of Al-O for Si-N in β-Si_3N_4 yields β-sialon with general formula: $Si_{6-x}Al_zO_zN_{8-z}$ ($0 < z < 4.2$). The structure is built up by Si and Al tetrahedra coordinated with oxygen and nitrogen. The unit cell contains two Si_3N_4 units. α-sialons are solid solutions based on the α-Si_3N_4 structure, with the general formula: $M^{p+}{}_xSi_{12-(m+n)}Al_{(m+n)}O_nN_{16-n}$, where **M** is metal ion such as Li, Ca, Ba, Y and RE with a valence of **p+** and index **m** = **px** [117].

[18] Yttria is often used additive to improve the sintering behavior of Si_3N_4 [124].

[19] In dependence on the system composition, the general composition of H-phase (N-apatite) can be written as $(M,REE)_{10}(SiO_4)_6N_2$. The specification of cations then leads to the names such as Mg-Nd-N-apatite [123].

[20] The melilite-type structure (tetragonal mineral melilite ($(Ca,Na)_2(Al,Mg,Fe^{2+})(Si,Al)_2O_7$)) is sorosilicate from the group of melilite, first described (Capo di Bove, near Rome, Italy) in 1976 and named from the Greek words *meli* "honey" and *lithos* "stone"). $Y_2Si_3O_3N_4$ was described by Fang et al [118]. N atoms fully occupy the bridging site (2*c*) and O atoms fully occupy the terminal site (4*e*) with 2 O and 6 N atoms at the bridging 8*f* site. The preferential distribution of O and N atoms at the 8*f* site results in two different local coordinations of Y and three different types of Si atoms.

Å and c = 6.355 Å. The electronic structure and bonding of the complex ceramic crystal $Y_{10}(SiO_4)_6N_2$ was studied by CHING et al [121]. This crystal is an insulator with direct band gap of 1.3 eV. It has some unique properties related to one-dimensional chain structure in the *c*-direction and planar N-Y bonding in the *x-y* plane.

The ternary phase diagrams of the Si_3N_4-Y_2O_3-SiO_2 [123] and Si_3N_4-La_2O_3-SiO_2 systems [129] are shown in **Fig. 29**(**a**) and (**b**). The apatite phase is able to form various solid solutions that may influence the development of strength in silicon nitride densified by yttria [130].

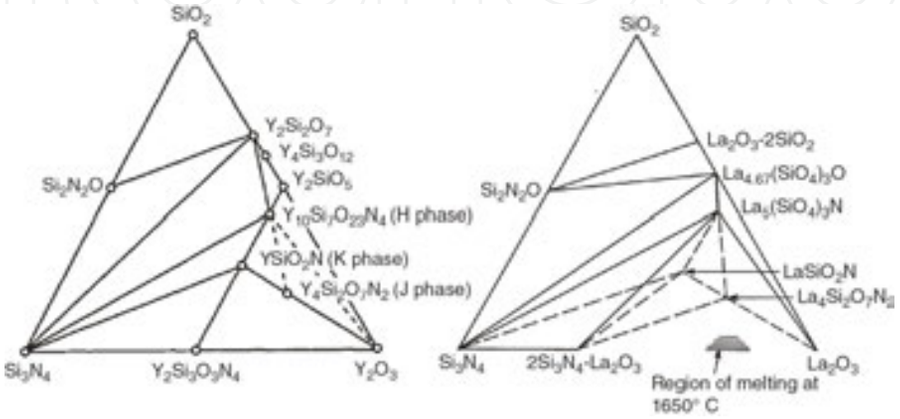

Fig. 29. Phase relationships in the systems Si_3N_4-SiO_2-Y_2O_3 [123] (a) and Si_3N_4-SiO_2-La_2O_3 at 1700°C and 1550°C (dashed lines) [129] (b).

The hexagonal lanthanum N-apatite phase of the composition of $La_5(SiO_4)_3N$ (isostructural with apatite) can be prepared from the mixture of La_2O_3 and Si powder sintered at temperatures in the range from 900 to 1200°C under the flow of nitrogen. The melting temperature of this phase was determined to be ~1600°C. It was observed that continuous heating and addition of Pd into the reaction mixture favored the formation of $La_5(SiO_4)_3N$. Prolonged heating of this compound yields $La_{4.67}(SiO_4)_3O$ [129],[131],[132],[133],[134],[135]. The absorption bands observed in infrared spectrum of lanthanum oxynitrides are introduced in **Table 4**.

Wavenumber [cm^{-1}]	**Mode**	**Frequency [cm^{-1}]**	**[cm^{-1}]**
225	δ (Si-O) (A_1)	730	ν (Si-N)
270	Si-O_2	800	SiO_2
327	δ (Si-O) (B_2)	840	Si-N
337	Si-O-Si (A_1)	872	SiO_4 (ν_1)
380	SiO_4 (ν_4)	909	ν (Si-N) vs
376 – 385	δ (Si-N) (sh)	930	Si-O-N_x
396	SiO_4 (ν_4)	940	ν Si-N vs
432	δ (Si-N) (sh)	960	
448	Si-N s or O-Si-O bend.	905	

Wavenumber [cm^{-1}]	Mode	Frequency [cm^{-1}]	[cm^{-1}]
462	SiO_4 (ν_4)	934	SiO_4 (s) (ν_3)
475		978	
490	ν Si-O (A_1)	980	ν Si-N (s)
542	ν Si-N (s)	1060	ν Si-O (ν_3)
600	ν Si-O	1090	ν Si-N (sh)
648	ν Si-O (w)	1130	ν Si-O (B_1)
679	ν Si-O m (B_2)	—	—

Table 4. The absorption bands observed in infrared spectrum of lanthanum oxynitrides [131].

Mitomo et al [129] used the mixture of Si_3N_4 and La_2O_3 powder heated in a 10 mm diameter carbon die using a hot-pressing apparatus. In some compositions and at temperatures above 1600°C, liquid phases were squeezed out of the die by applied pressure resulting in a change in the overall composition. The compacted powder was therefore heated at the pressure of 20 MPa up to 1400°C and the temperature was then raised to 1700°C without the pressure. The specimen was kept at 1700°C for 1 h and then allowed to cool.

The sintering temperature of Si_3N_4 with La_2O_3 additions is 1700 to 1800°C. Heating of powder mixture of various Si_3N_4/L_2O_3 ratios at 1700°C results in the formation of $2Si_3N_4{\cdot}La_2O_3$, $La_5(SiO_4)_3N$[21] and β-Si_3N_4 or a glass. The reactions occurring during heating were determined as follows [129]:

$$\begin{aligned} Si_3N_4 + La_2O_3 &\xrightarrow{1200-1250^\circ C} Si_3N_4 + \left(La_4Si_2O_7N_2 + LaSiO_2N\right) \\ &\xrightarrow{1400-1500^\circ C} LaSiO_2N + Si_3N_4 \\ &\xrightarrow{1650-1750^\circ C} 2\,Si_3N_4 \cdot La_2O_3 + \text{liquid} \\ &\xrightarrow{20^\circ C} 2\,Si_3N_4 \cdot La_2O_3 + La_5(SiO_4)_3N + \text{glass} \end{aligned} \tag{14}$$

The results of Sakai et al [136] indicate that N-apatite and N-diopside containing grain boundary phase may improve the oxidation resistance of silicon nitride. Since the oxidation of Si_3N_4 leads to the formation of protective SiO_2 layer on the surface:

$$Si_3N_4 + 3\ O_2 \rightarrow 3\ SiO_2 + 2\ N_2 \tag{15}$$

[21] The presence of $La_5(SiO_4)_3N$ is inevitable in the production of high-density materials by liquid-phase sintering; therefore, the amount of $La_5(SiO_4)_3N$ and glassy phase must be minimized to obtain materials with good high-temperature strengths [129].

the silicon nitride shows excellent oxidation resistance. Formed SiO_2 then reacts with the grain boundary constituents to form silicates:

$$SiO_2 + MeO_x \rightarrow MeSiO_{2+x} \tag{16}$$

but in the case of MgO, the formed layer did not act as protection [136]. $Y_{4.67}(SiO_4)_3O$ apatite (britholite phase[2]) is formed as the oxidation product of silicon yttrium oxynitride (H-phase) in the temperature range from 700 to 1400°C [137],[138].

5.6. REE vanadocalcic apatite

The synthesis and physicochemical study of rare-earth-containing vanadocalcic oxyapatites where the pair Ca^{2+} and □ was substituted by Ln^{3+} and $1/2O^{2-}$ was described by Benmoussa et al [139]. This substitution leads to lanthanum and praseodymium dioxyapatites $Ca_8Ln_2(VO_4)_6O_2$, where Ln = La and Pr. Regarding rare earths such as neodymium, samarium, europium, gadolinium and terbium, the Ln^{3+} content limit varies from one REE to another. It decreases when the REE ionic radius declines.

5.7. Apatite-type yttrium phosphates

The following compositions having the apatite structure were prepared by Wanmaker et al [140]:

a. $Me(II)_{2+x}Me(III)_{8-x}(SiO_4)_{6-x}(PO_4)_xO_2$, where $0 \leq x \leq 6$;

b. $Me(II)_{3+x}MeIII_{6-x}(SiO_4)_{6-x}(PO_4)_x$, where $0 \leq x \leq 1.5$;

c. $Me(II)_{4+x}Me(III)_{6-x}(SiO_4)_{6-x}(PO_4)_xO$, where $0 \leq x \leq 6$.

with Me(II) = Ca, Sr, Ba, Mg, Zn or Cd and Me(III) = Y or La. Among these, there are several new compounds, e.g. $Zn_2La_8(SiO_4)_6O_2$, $BaMgY_8(SiO_4)_6O_2$, $Zn_2Y_8(SiO_4)_6O_2$, $Cd_2Y_8(SiO_4)_6O_2$, $Ca_4La_5(SiO_4)_5(PO_4)$ and $Ba_4La_5(SiO_4)_5(PO_4)$. The crystallographic parameters were determined and their luminescence was studied. The most efficient activator proved to be trivalent antimony, especially in the compositions of type I. At 77°K, an emission band at about 400 nm was observed in many of these apatites.

The humidity-sensitivity of yttrium-substituted calcium oxyhydroxyapatites was studied by Owada et al [141]. The logarithm of the electrical resistance of present sensors decreased linearly with increasing relative humidity (RH) from 30 to 65%. The resistance of $[Ca_{9.0}Y_{1.0}](PO_4)_6[O_{1.5}□_{0.5}]$ with the largest OH vacancy content was about one order of magnitude lower than that of calcium hydroxyapatite. It was found that the larger the ratio of surface hydroxyl groups per unit surface area in the sample, the lower the resistance and the higher the amount of OH vacancies.

A ceramic proton conductor was obtained in the solid solutions of yttrium-substituted oxyhydroxyapatite $(Ca_{10-x}Y_x)(PO_4)_6((OH)_{2-x-2y}O_{x+y}\square_y)$ [142]. Using the hydrogen concentration cells, it was confirmed that the specimens with the composition of $x \leq 0.65$ have the protonic transference number (t_i) is equal to one, while the values of t_i of specimens with $0.65 < x < 1$ were smaller than one. The conduction properties were also dependent on the composition of apatites. At $x = 0.65$, the conductivity (σ) showed the maximum value ($5 \cdot 10^{-4} S \cdot cm^{-1}$ at 800°C) in the relationship between σ and x, while the activation energy was the lowest (about 1.0 eV) at corresponding x. The applicability of proton conductive apatite for a fuel cell was discussed in **Section 10.4**.

Author details

Petr Ptáček

Brno University of Technology, Czech Republic

References

[1] Richards R. Surface and Nanomolecular Catalysis. CRC Press, 2006. ISBN: 978-1420015751

[2] Kendrick E, Slater PR. Synthesis of Ga-doped Ge-based apatites: Effect of dopant and cell symmetry on oxide ion conductivity. Materials Research Bulletin 2008;43(12) 3627–3632.

[3] Xiang J, Liu Zhan-G, Ouyang Jia-H, Yan Fu-Y. Synthesis, structure and electrical properties of rare-earth doped apatite-type lanthanum silicates. Electrochimica Acta 2012;65 251–256.

[4] Fuentes AF, Rodríguez-Reyna E, Martínez-González LG, Maczka M, Hanuza J, Amador U. Room-temperature synthesis of apatite-type lanthanum silicates by mechanically milling constituent oxides. Solid State Ionics 2006;177(19-25) 1869–1873.

[5] Tao Sh, Irvine JTS. Preparation and characterisation of apatite-type lanthanum silicates by a sol-gel proces. Materials Research Bulletin 2001;36(7-8) 1245–1258.

[6] Martínez-González LG, Rodríguez-Reyna E, Moreno KJ, Escalante-García JI, Fuentes AF. Ionic conductivity of apatite-type rare-earth silicates prepared by mechanical milling. Journal of Alloys and Compounds 2009; 476(1-2) 710–714.

[7] Parmentier J, Liddell K, Thompson DP, Lemercier H, Schneider N, Hampshire S, Bodart PR, Harris RK. Influence of iron on the synthesis and stability of yttrium silicate apatite. Solid State Sciences 2001;3(4) 495–502.

[8] Hamon C, Marchand R, Maunaye M, Gaudé J, Guyader J. Revue de chimie minérale 1975;12 259.

[9] Kuzmin EA, Belov NV. Doklady Akademii Nauk SSSR 1965;165 88.

[10] Felsche J. Naturwissenschaften 1967;29 325.

[11] McCarthy GJ, White WB, Roy RJ. Preparation of $Sm_4(SiO_4)_3$. Journal of Inorganic and Nuclear Chemistry 1967;29 253–254.

[12] Higuchi M, Masubuchi Y, Nakayama S, Kikkawa S, Kodaira K. Single crystal growth and oxide ion conductivity of apatite-type rare-earth silicates. Solid State Ionics 2004;174(1-4) 73–80.

[13] Arrhenius SA. Über die Dissoziationswärme und den Einfluss der Temperatur auf den Dissociationsgrad der Elektrolyte. Zeitschrift für Physikalische Chemie 1889;4 96–116.

[14] Arrhenius , SA. Über die Reaktionsgeschwindigkeit bei der Inversion von Rohrzucker durch Säuren. Zeitschrift für Physikalische Chemie 1889;4: 226–248.

[15] Clugston M, Flemming R. Advanced Chemistry. A New Mainstream Text for the New Specifications, Advanced Science. OUP Oxford, 2000. ISBN: 978-0199146338

[16] Shi Q, Zhang H. Electrical properties of iron doped apatite-type lanthanum silicates. Journal of Rare Earths 2012;30(12) 1235–1239.

[17] Takeda N, Itagaki Y, Aono H, Sadaoka Y. Preparation and characterization of $Ln_{9.33+x/3}Si_{6-x}Al_xO_{26}$ (Ln = La, Nd and Sm) with apatite-type structure and its application to a potentiometric O_2 gas sensor. Sensors and Actuators B: Chemical 2006;115(1) 455–459.

[18] El-Batanouny M, Wooten F. Symmetry and Condensed Matter Physics: A Computational Approach. Cambridge University Press, 2008. ISBN: 978-1139469517

[19] Lambert S, Vincent A, Bruneton E, Beaudet-Savignat S, Guillet F, Minot B, Bouree F. Structural investigation of $La_{9.33}Si_6O_{26}$- and $La_9AESi_6O_{26+\delta}$-doped apatites-type lanthanum silicate (AE = Ba, Sr and Ca) by neutron powder diffraction. Journal of Solid State Chemistry 2006;179(8) 2602–2608.

[20] Fukuda K, Asaka T, Okino M, Berghout A, Béchade E, Masson O, Julien I, Thomas P. Anisotropy of oxide-ion conduction in apatite-type lanthanum silicate. Solid State Ionics 2012;217 40–45.

[21] Sumathi S, Buvaneswari G. Synthesis of apatite structure based $BiNaCa_3(PO_4)_3OH$ and its application for condensation reaction. Ceramics International 2012;38(5) 3547–3552.

[22] Kiyono H, Matsuda Y, Shimada T, Ando M, Oikawa I, Maekawa H, Nakayama S, Ohki S, Tansho M, Shimizu T, Florian P, Massiot D. Oxygen-17 nuclear magnetic resonance measurements on apatite-type lanthanum silicate ($La_{9.33}(SiO_4)_6O_2$). Solid State Ionics 2012;228 64–69.

[23] Harman G. Wire Bonding in Microelectronics 3 Edition by George Harman: Wire Bonding in Microelectronics. McGraw-Hill Professional, 2010. ISBN: 978-0-07-164265-1.

[24] Abram EJ, Kirk CA, Sinclair DC, West AR. Synthesis and characterisation of lanthanum germanate-based apatite phases. Solid State Ionics 2005;176(23-24) 1941–1947.

[25] Shaula AL, Kharton VV, Waerenborgh JC, Rojas DP, Marques FMB. Oxygen ionic and electronic transport in apatite ceramics. Journal of the European Ceramic Society 2005;25(12) 2583–2586.

[26] Shaula AL, Kharton VV, Marques FMB. Oxygen ionic and electronic transport in apatite-type $La_{10-x}(Si,Al)_6O_{26\pm\delta}$. Journal of Solid State Chemistry 2005;178(6) 2050–2061.

[27] Shaula AL, Kharton VV, Marques FMB. Ionic and electronic conductivities, stability and thermal expansion of $La_{10-x}(Si,Al)_6O_{26\pm\delta}$ solid electrolytes. Solid State Ionics 2006;177(19-25) 1725–1728.

[28] Helfferich FG. Ion Exchange. Dover Science Books. McGraw-Hill Series in Advanced Chemistry. Courier Corporation, 1962. ISBN: 978-0486687841

[29] Abram EJ, Sinclair DC, West AR. A novel enhancement of ionic conductivity in the cation-deficient apatite $La_{9.33}(SiO_4)_6O_2$. Journal of Material Chemistry 2001;11 1978–1979.

[30] Kharton VV, Marques FMB, Atkinson A. Transport properties of solid oxide electrolyte ceramics: a brief review. Solid State Ionics 2004;174(1-4) 135–149.

[31] Mössbauer RL. Kernresonanzfluoreszenz von Gammastrahlung in Ir191. Zeitschrift für Physik A 1958;151(2) 124–143.

[32] Greenwood NN. Mössbauer Spectroscopy. Springer Science & Business Media, 2012. ISBN: 978-9400956971

[33] Dickson PE, Berry FJ. Mössbauer Spectroscopy. Cambridge University Press, 2005. ISBN: 978-0521018104

[34] Miglierini M, Petridis D. Mössbauer Spectroscopy in Materials Science. Nato Science Partnership Subseries: 3 — Volume 66. Springer Science & Business Media, 2013. ISBN: 978-9401145480

[35] Yaremchenko AA, Shaula AL, Kharton VV, Waerenborgh JC, Rojas DP, Patrakeev MV, Marques FMB. Ionic and electronic conductivity of $La_{9.83-x}Pr_xSi_{4.5}Fe_{1.5}O_{26\pm\delta}$ apatites. Solid State Ionics 2004;171(1-2) 51–59.

[36] Yoshioka H, Nojiri Y, Tanase Sh. Ionic conductivity and fuel cell properties of apatite-type lanthanum silicates doped with Mg and containing excess oxide ions. Solid State Ionics 2008;179(30) 2165–2169.

[37] Yuan W, Gu Y, Li L. Synthesis and ionic conduction of cation-deficient apatite $La_{9.33-2x/3}M_xSi_6O_{26}$ doped with Mg, Ca, Sr*. Chinese Journal of Chemical Engineering 2008;16(3) 488–491.

[38] Irvine JTS, Corcoran DJD, Cull PA. Structure and ionic conduction in solids. Nordic Workshop on Materials for Electrochemical Conversion, Geilo Norway 2000; 37-41.

[39] Hosseini SM, Shvareva T, Navrotsky A. Energetics of lanthanum silicate apatite: Influence of interstitial oxygen and cation vacancy concentrations in $La_{9.33+x}(SiO_4)_6O_{2+3x/2}$ and $La_{10-x}Sr_x(SiO_4)_6O_{3-0.5x}$. Solid State Ionics 2013;233 62–66.

[40] Karato S. Deformation of Earth Materials: An Introduction to the Rheology of Solid Earth. Cambridge University Press, 2008. ISBN: 978-1139469562

[41] Kong LB, Huang YZ, Que WX, Zhang TS, Li S, Zhang J, Dong ZL, Tang DY. Transparent Ceramics. Topics in Mining, Metallurgy and Materials Engineering. Springer, 2015. ISBN: 978-3319189567

[42] Chung Yip-W. Introduction to Materials Science and Engineering. CRC Press, 2006. ISBN: 978-0849392634

[43] Kosevich AM. The Crystal Lattice: Phonons, Solitons, Dislocations, Superlattices. John Wiley & Sons, 2006. ISBN: 978-3527606931

[44] Tao Sh, Irvine JTS. Preparation and characterization of apatite-type lanthanum silicates by a sol-gel proces. Materials Research Bulletin 2001;36(7-8) 1245–1258.

[45] Li B, Liu W, Pan W. Synthesis and electrical properties of apatite-type $La_{10}Si_6O_{27}$. Journal of Power Sources 2010;195(8) 2196–2201.

[46] Masubuchi Y, Higuchi M, Takeda T, Kikkawa Sh. Preparation of apatite-type $La_{9.33}(SiO_4)_6O_2$ oxide ion conductor by alcoxide-hydrolysis. Journal of Alloys and Compounds 2006;408-412 641-644.

[47] Sansom JEH, Sermon PA, Slater PR. Synthesis and conductivities of the Ti doped apatite-type phases $(La/Ba)_{10-x}(Si/Ge)_{6-y}Ti_yO_{26+z}$. Solid State Ionics 2005;176(19-22) 1765–1768.

[48] Yuan W, Gu Y, Li L. Synthesis and conductivity of oxyapatite ionic conductor $La_{10-x}V_x(SiO_4)_6O_{3+x}$. Chinese Journal of Chemical Engineering 2010;18(2) 328–332.

[49] Mazza D, Tribaudino M, Delmastro A, Lebech B. Synthesis and neutron diffraction study of $La_5Si_2BO_{13}$, an analog of the apatite mineral. Journal of Solid State Chemistry 2000;155(2) 389–393.

[50] Arbib EH, Eloudi E, Chaminade JP, Darriet J. The crystal structure of the phosphate eulytite $Ba_3Bi(PO_4)_3$. Materials Research Bulletin 2000;35(5) 761–773.

[51] Naidu SA, Varadaraju UV, Raveau B. Eu^{3+} luminescence in $La_5Si_2BO_{13}$ with apatite related structure and magnetic studies in $Ln_5Si_2BO_{13}$ (Ln=Gd, Dy). Journal of Solid State Chemistry 2010;183(8) 1847–1852.

[52] Vieira MM, Oliveira JC, Shaula AL, Trindade B, Cavaleiro A. Structure and ionic conductivity of reactively sputtered apatite-type lanthanum silicate thin films. Surface and Coatings Technology 2014;247 14–19.

[53] Wang Shou-Q, Uda S. Phase relations around langasite ($La_3Ga_5SiO_{14}$) in the system La_2O_3-Ga_2O_3-SiO_2 in air. Journal of Crystal Growth 2003;250(3-4) 463–470.

[54] El Ouenzerfi R, Goutaudier C, Panczer G, Moine B, Cohen-Adad MT, Trabelsi-Ayedi M, Kbir-Ariguib N. Investigation of the CaO-La_2O_3-SiO_2-P_2O_5 quaternary diagram. Synthesis, existence domain, and characterization of apatitic phosphosilicates. Solid State Ionics 2003;156(1-2) 209–222.

[55] Wanmaker WL, ter Vrugt JW, Verlijsdonk JG. Luminescence of alkaline earth yttrium and lanthanum phosphate-silicates with apatite structure. Journal of Solid State Chemistry 1971;3(3) 452–457.

[56] Bonhomme C, Beaudet-Savignat S, Chartier Th, Maître A, Sauvet Anne-L, Soulestin B. Sintering kinetics and oxide ion conduction in Sr-doped apatite-type lanthanum silicates, $La_9Sr_1Si_6O_{26.5}$. Solid State Ionics 2009;180(36-39) 1593–1598,

[57] Mazza D, Ronchetti S. Study on the Al_2O_3-SiO_2-La_2O_3 ternary system at 1300°C. Materials Research Bulletin 1999;34(9) 1375–1382.

[58] Kuz'min VN, Belov KP. Doklady Akademii Nauk SSSR 1965;165, 88.

[59] McCarthy GJ, White WB, Roy R. Preparation of $Sm_4(SiO_4)_3$. Journal of Inorganic and Nuclear Chemistry 1967;29(1) 253–254.

[60] Felsche J. Naturwissenschaften 1969;56 325.

[61] Nakayama S, Sakamoto M. Preparation of apatite-type $La_{9.33}Ge_6O_{26}$ single-crystal from sintered ceramics by a seeding method and its oxide ionic conduction. Solid State Ionics 2013;253 47–52.

[62] Kendrick E, Slater PR. Synthesis of hexagonal lanthanum germanate apatites through site selective isovalent doping with yttrium. Materials Research Bulletin 2008;43(8-9) 2509–2513.

[63] Najib A, Sansom JE, Tolchard JR, Slater PR, Islam MS. Doping strategies to optimise the oxide ion conductivity in apatite-type ionic conductors. Dalton Transactions 2004;7(19) 3106–3109.

[64] Orera A, Headspith D, Apperley DC, Francesconi MG, Slater PR. Formation of apatite oxynitrides by the reaction between apatite-type oxide ion conductors, $La_{8+x}Sr_{2-x}(Si/Ge)_6O_{26+x/2}$, and ammonia. Journal of Solid State Chemistry 2009;182(12) 3294–3298.

[65] Emirdag-Eanes M, Pennington WT, Kolis JW. Synthesis, structural characterization, and magnetic properties of $NaRE_9(GeO_4)_6O_2$ (RE = Nd, Pr). Journal of Alloys and Compounds 2004;366(1-2) 76–80.

[66] Takahashi M, Uematsu K, Ye Zuo-G, Sato M. Single-crystal growth and structure determination of a new oxide apatite, $NaLa_9(GeO_4)_6O_2$. Journal of Solid State Chemistry 1998;139(2) 304–309.

[67] Chen P, Li RK. Two high terbium content apatites: $Tb_5Si_2BO_{13}$ and $Tb_{4.66}Si_3O_{13}$. Journal of Alloys and Compounds 2015;622 859–864.

[68] Xia MJ. Li RK. Structure and optical properties of a noncentrosymmetric borate $RbSr_4(BO_3)_3$. Journal of Solid State Chemistry 2013;197 366–369.

[69] Kazmierczak K, Höppe HA. Synthesis, crystal structure and optical spectra of europium borate fluoride $Eu_5(BO_3)_3F$. European Journal of Inorganic Chemistry 2010;18 2678–2681.

[70] Chen S, Hoffmann S, Carrillo-Cabrera W, Akselrud LG, Prots Y, Schwarz U, Zhao Jing-T, Kniep R. $Sr_{10}[(PO_4)_{5.5}(BO_4)_{0.5}](BO_2)$: Growth and crystal structure of a strontium phosphate orthoborate metaborate closely related to the apatite-type crystal structure. Journal of Solid State Chemistry 2010;183(3) 658–661.

[71] Yu Y, Wu QS, Li RK. Structure of two new borates $YCa_3(AlO)_3(BO_3)_4$ and $YCa_3(GaO)_3(BO_3)_4$. Journal of Solid State Chemistry 2006;179(2) 429–432.

[72] Kim HK, Ao Sio-I, Rieger BB. IAENG Transactions on Engineering Technologies: Special Edition of the World Congress on Engineering and Computer Science 2011. Springer Science & Business Media, 2012. ISBN: 978-9400747852

[73] Khomskii D. Transition Metal Compounds. Cambridge University Press, 2014. ISBN: 978-1107020177

[74] Lacroix C, Mendels P, Mila F. Introduction to Frustrated Magnetism: Materials, Experiments, Theory. Springer Series in Solid-State Sciences — Volume 164. Springer Science & Business Media, 2011. ISBN: 978-3642105890

[75] Werner F, Kubel F. Apatite-type $Pr_9K(SiO_4)_6O_2$ — A potential oxide ion conductor. Materials Letters 2005;59(28) 3660–3665.

[76] Morgan MG, Wang M, Mar A. Samarium orthosilicate oxyapatite, $Sm_5(SiO_4)_3O$. Acta Crystallographica Section E, 2010. DOI: 10.1107/S1600536802011868

[77] Sakakura T, Kamoshita M, Iguchi H, Wang J, Ishizawa N. Apatite-type $SrPr_4(SiO_4)_3O$. Crystallographica Section E, 2010. DOI: 10.1107/S1600536810033349

[78] Felsche J. Rare earth silicates with the apatite structure. Journal of Solid State Chemistry 1972;5(2) 266–275.

[79] Xiang J, Liu Zhan-G, Ouyang Jia-H, Zhou Y, Yan Fu-Y. Influence of doping with various cations on electrical conductivity of apatite-type neodymium silicates. Ceramics International 2013; 39(5) 4847–4851.

[80] Latshaw AM, Smith MD, zur Loye Hans-C. Crystal growth and structure of three new neodymium containing silicates: $Na_{0.50}Nd_{4.50}(SiO_4)_3O$, $Na_{0.63}Nd_{4.37}(SiO_4)_3O_{0.74}F_{0.26}$ and $Na_{4.74}Nd_{4.26}(O_{0.52}F_{0.48})[SiO_4]_4$. Solid State Sciences 2014;35 28–32.

[81] Wang Ch, Liu X, Fleet ME, Feng Sh , Xu R. High-pressure synthesis and single-crystal structure refinement of gadolinium holmium silicate hydroxyapatite $Gd_{4.33}Ho_{4.33}(SiO_4)_6(OH)_2$. Journal of Solid State Chemistry 2006;179(7) 2245–2250.

[82] Haile SM, Wuensch BJ, Siegrist T, Laudise RA. Hydrothermal synthesis of new alkali silicates I. Potassium neodymium phases. Journal of Crystal Growth 1993;131(3-4) 352–372.

[83] Haile SM, Wuensch BJ, Laudise RA. Hydrothermal synthesis of new alkali silicates II. Sodium neodymium and sodium yttrium phases. Journal of Crystal Growth 1993;131(3-4) 373–386.

[84] Boughzala K, Salem BE, Chrifa AB, Gaudin E, Bouzouita K. Synthesis and characterization of strontium-lanthanum apatites. Materials Research Bulletin 2007;42(7) 1221–1229.

[85] Małecka MA, Kępiński L. Synthesis and structure of nanocrystalline mixed Ce-Yb silicates. Materials Research Bulletin 2013;48(7) 2571–2577.

[86] Xiang J, Ouyang Jia-H, Liu Zhan-G. Microstructure and electrical conductivity of apatite-type $La_{10}Si_{6-x}WxO_{27+\delta}$ electrolytes. Journal of Power Sources 2015;284 49–55.

[87] Wang Sea-F, Hsu Yung-F, Lin Wan-J. Effects of Nb^{5+}, Mo^{6+}, and W^{6+} dopants on the germanate-based apatites as electrolyte for use in solid oxide fuel cells. International Journal of Hydrogen Energy 2013;38(27) 12015–12023.

[88] Institut kristallografii im. Shubnikova AV, Sheftal' NN. Growth of Crystals, Volume 6, Part 1. Consultants Bureau, 1965.

[89] Toropov NA, Bondar IA. In: Levin EM, Robbins CR, McMurdie HF (Eds.), Phase Diagrams for Ceramists, 1969.

[90] Toporov NA, Fedorov NF. Composition diagram of the Ca_2SiO_4-$Y_4(SiO_4)_3$ system. Zhurnal Neorganicheskoi Khimii 1965;10 666–668.

[91] Laczai N, Péter Á, Kovács L, Bencs L, Lőrincz E. Synthesis and characterization of $Y_2(SiO_4)O$:Ce with LiF and NaF additives. Solid State Sciences 2015;45 23–29.

[92] Mao H, Selleby M, Fabrichnaya O. Thermodynamic reassessment of the Y_2O_3-Al_2O_3-SiO_2 and its subsystems. Calphad 32 399-412. DOI: 10.1016/j.calphad.2008.03.003.

[93] Liddell K, Thompson DP. X-ray diffraction data for yttrium silicates. British Ceramic Transactions 1986;85 17–22.

[94] Warshaw I, Roy R. In: Progress in Science and Technology of Rare Earths, Vol. 1. New York: Pergamum Press, 1964, p. 203.

[95] Ito J, Johnson H. Synthesis and study of yttrialite. American Mineralogist 1968;53 1940–1952.

[96] Escudero A, Alba MD, Becerro AI. Polymorphism in the $Sc_2Si_2O_7$-$Y_2Si_2O_7$ system. Journal of Solid State Chemistry 2007;180 1436–1445.

[97] Wills RR, Cunningham JA, Wimmer JM, Stewart RW. Stability of the silicon yttrium oxynitrides. Journal of the American Ceramic Society 1976;59(5-6) 269–270.

[98] Cannas C, Musinu A, Piccaluga G, Deidda C, Serra F, Bazzoni M, Enzo S. Advances in the structure and microstructure determination of yttrium silicates using the Rietveld method. Journal of Solid State Chemistry 2005;178(5) 1526–1532.

[99] McColm I. Dictionary of Ceramic Science and Engineering. 2nd ed., Springer Science & Business Media, 2013. ISBN: 978-1475723212

[100] Suwa Y, Naka S, Noda T. Preparation and properties of yttrium magnesium silicate with apatite structure. Materials Research Bulletin 1968;3(2) 139–147.

[101] Lee FC, Marr J, Glasser FP. Compounds in the $Na_2O{\cdot}Y_2O_3{\cdot}SiO_2$ system. Ceramics International 1981;7(2) 43–47.

[102] Bondar IA, Galakhov FY. Izvestiya Akademii Nauk: Seriya Khimicheskaya 1964;7 1325–1326.

[103] Shannon RD. Revised effective ionic radii and systematic studies of interatomic distances in halides and chalcogenides. Acta Crystallographica Section A 1976;32(5) 751–767.

[104] Brown ID, Altermatt D. Bond-valence parameters obtained from a systematic analysis of the inorganic crystal structure database. Acta Crystallographica Section B 1985;41 244–247.

[105] Wills RR, Cunningham JA, Wimmer JM, Stewart RW. Stability of the silicon yttrium oxynitrides. Journal of the American Ceramic Society 1976;59(5-6) 269–270.

[106] Rakovan JF, Hughes JM. Strontium in the apatite structure: Strontian fluorapatite and belovite-(Ce). The Canadian Mineralogist 2000;38 839–845.

[107] Zuev MG, Karpov AM, Shkvarin AS. Synthesis and spectral characteristics of $Sr_2Y_8(SiO_4)_6O_2$: Eu polycrystals. Journal of Solid State Chemistry 2011;184(1) 52–58.

[108] Karpov AM, Zuev MG. Sol-gel synthesis and spectral characteristics of crystal phosphors $Sr_2Y_{8(1-x)}Eu_{8x}Si_6O_{26}$. Glass Physics and Chemistry 2012;38(4) 431–436.

[109] Holand W, Beall GH. Glass Ceramic Technology. 2nd ed., John Wiley & Sons, 2012. ISBN: 978-1118265925

[110] Ahlborg NL, Zhu D. Calcium-Magnesium-Aluminosilicate (CMAS) Reactions and Degradation Mechanisms of Advanced Environmental Barrier Coatings. National Aeronautics and Space Administration. NASA/TM-2013-218091

[111] Li G, Zhang Y, Geng D, Shang M, Peng C, Cheng Z, Lin J. Single-composition trichromatic white-emitting $Ca_4Y_6(SiO_4)_6O$: $Ce^{3+}/Mn^{2+}/Tb^{3+}$ phosphor: Luminescence and energy transfer. ACS Applied Materials & Interfaces 2012;4(1) 296–305.

[112] Wanmaker WL, Vrugt JW, Verlijsdonk JG. Synthesis of new compounds with apatite structure. Philips Research Reports 1971;26 373–381.

[113] van't Hoen C, Rheinberger V, Höland W, Apel E. Crystallization of oxyapatite in glass-ceramics. Journal of the European Ceramic Society 2007;27(2-3) 1579–1584.

[114] Gunawardane RP, Howie RA, Glasser FP. Structure of the oxyapatite $NaY_9(SiO_4)_6O_2$. Acta Crystallographica Section B 1982;38(5) 1564–1566.

[115] Redhammer GR, Roth G. Lithium and sodium yttrium orthosilicate oxyapatite, $LiY_9(SiO_4)_6O_2$ and $NaY_9(SiO_4)_6O_2$, at both 100 K and near room temperature. Acta Crystallographica Section C 2003;59(12) 120–124.

[116] Ptáček P, Bartoníčková E, Švec J, Opravil T, Šoukal F, Wasserbauer J, Másilko J. Preparation, kinetics of sinter-crystallization and properties of hexagonal strontium-yttrate-silicate apatite phase: $SrY_4[SiO_4]_3O$. Ceramics International 2015;41(1) 1779–1795.

[117] Heimann RB. Classic and Advanced Ceramics: From Fundamentals to Applications. Vydavatel John Wiley & Sons, 2010. ISBN: 978-3527630189

[118] Fang CM, de Wijs GA, de Groot RA, Metselaar R, Hintzen HT, de With G. O/N ordering in $Y_2Si_3O_3N_4$ with the melilite-type structure from first-principles calculations. Chemistry of Materials 2000;12(4) 1071–1075.

[119] Liddell K, Mandal H, Thompson DP. X-ray data for new Y-Si-Al-O-N glass ceramics. Journal of the European Ceramic Society 1997;17(6) 781–877.

[120] Ahmad S, Ludwig T, Herrmann M, Mahmoud MM, Lippmann W, Seifert HJ. Crystallisation studies of Si_3N_4-Al_2O_3-SiO_2-Y_2O_3 glass-ceramics under different heat-treatment conditions. Journal of the European Ceramic Society 2015;35(8) 2261–2268.

[121] Ching Wai-Y, Xu Yong-Ni, Ouyang L. Electronic structure and bonding in crystalline $Y_{10}[SiO_4]_6N_2$. Journal of the American Ceramic Society 2004;86(8) 1424–1426.

[122] Riedel R, Chen I-W. Ceramics Science and Technology, Structures. Ceramics Science and Technology — Volume 1. John Wiley & Sons, 2011. ISBN: 978-3527631933.

[123] Alper AM (Ed.), Kostorz G, Herman H. Phase Diagrams in Advanced Ceramics. Treatise on Materials Science and Technology. Elsevier, 1995. ISBN: 978-0080538723

[124] Jansen M (Ed.), Haubner R, Herrmann M, Lux B, Petzow G, Weissenbacher R, Wilhelm M. High Performance Non-Oxide Ceramics II. Structure and Bonding — Volume 102. Springer, 2003. ISBN: 978-3540456230

[125] Alper AM. Phase Diagrams: Materials Science and Technology, In: Alper AM (Ed.), Volume 6, Part 5. Academic Press, 1978. ISBN: 978-0120532032

[126] Rae AWJ, Thompson DP, Pikin NJ, Jack KH. pp. 347-360 In: Poper P (Ed.), Special Ceramics. British Ceramic Research Association, Stoke-on Trent, England, D.P. Thompson, p. 358, 1975.

[127] Wills RR, Holmquist S, Wimmer JM, Cunningham JA. Phase relationships in the system SiO_2-Y_2O_3-Si_3N_4. Journal of Materials Science 1976;11(7) 1305–309.

[128] Gauckler LJ, Hohnke H, Tien TY. The system Si_3N_4-SiO_2-Y_2O_3. Journal of the American Ceramic Society 1980;63(1-2) 35–37.

[129] Mitomo M, Izumi F, Haruichi S, Matsui Y. Phase relationships in the system Si_3N_4-SiO_2-La_2O_3. Journal of Materials Science 1982;17(8) 2359–2369.

[130] Buhl H. Advanced Aerospace Materials. Materials Research and Engineering. Springer Science & Business Media, 2012. ISBN: 978-3642501593

[131] Kizilyalli M, Gürbüz G. Lanthanum silicon oxynitrides, synthesis and X-ray diffraction and IR studies. Find out how to access preview-only content. NATO ASI Series 1990;185 45–67.

[132] Lange FF. Si_3N_4-Ce_2O_3-SiO_2 materials: Phase relations and strength. American Ceramic Society Bulletin 1980;59(2) 239–240.

[133] Thompson DP. Special Ceramics 1975;358.

[134] Mitomo N, Kuramoto N, Suzuki H. Journal of Materials Science Letters 1978;13 2523.

[135] Gaude J, Guyader J, Lang J. Comptes Rendus de l'Académie des Sciences, Serie C 1975;280 883–884.

[136] Sakai H, Soma T. Matsui M, Oda I. Oxidation and microstructure of sintered silicon nitride. In: Pask JA, Evans AG (Eds.). Ceramic Microstructures '86: Role of Interfaces, Materials Science Research — Volume 21. Springer Science & Business Media, 2013. ISBN: 978-1461319337

[137] International Aerospace Abstracts, Volume 33, Edition 4-6. American Institute of Aeronautics and Astronautics. Technical Information Service, Cambridge Scientific Abstracts, Inc., United States. National Aeronautics and Space Administration, Institute of the Aerospace Sciences. Technical Information Service, American Institute of Aeronautics and Astronautics, 1993.

[138] Physics Soviet, Crystallography, Volume 14, Pages 1-484. American Institute of Physics, American Crystallographic Association. American Institute of Physics, 1969.

[139] Benmoussa H, Mikou M, Lacout JL. Synthesis and physicochemical study of new rare-earth-containing vanadocalcic oxyapatites. Materials Research Bulletin 1999;34(9) 1429–1434.

[140] Wanmaker WL, ter Vrugt JW, Verlijsdonk JG. Luminescence of alkaline earth yttrium and lanthanum phosphate-silicates with apatite structure. Journal of Solid State Chemistry 1971;3(3) 452–457.

[141] Owada H, Yamashita K, Umegaki T, Kanazawa T, Nagai M. Humidity-sensitivity of yttrium substituted apatite ceramics. Solid State Ionics 1989;35(3-4) 401–404.

[142] Yamashita K, Owada H, Umegaki T, Kanazawa T, Katayama K. Protonic conduction in yttrium-substituted hydroxyapatite ceramics and their applicability to H_2-O_2 fuel cell. Solid State Ionics 1990;40-41(2) 918-921.